Chapter 1   Introduction

1.1 Properties of the ZnO

ZnO with hexagonal wurtzite structure (lattice constants a = 3.2438 and c = 5.2036 Å as shown in Fig. 1-1.1) has many attractive properties such as direct wide band gap (E_g = 3.3 eV) and large exciton binding energy (~60 meV) at room temperature, significantly larger than that of ZnSe (22 meV) and GaN (25 meV), native tendency of *n*-type electric property, piezoelectricity, and transparency. These properties make ZnO thin film a potential material for many applications such as the ultraviolet light emitters[1, 2], piezoelectric transducers[3], transparent electronics[4-6], surface acoustic wave devices[7], and solar cells[8, 9]. But the ZnO films are required to have high crystal quality for most applications. So we choose the c-plane sapphire as the substrate. The c-plane sapphire (α-Al_2O_3 with a rhombohedral crystal structure and lattice constants a = 4.7588Å and c = 12.992Å) is commonly adopted as the substrate for ZnO growth because the reasonable costs and good quality of ZnO obtained. On c-sapphire, ZnO preferentially grows with its c-axis aligned with the c-axis of sapphire.
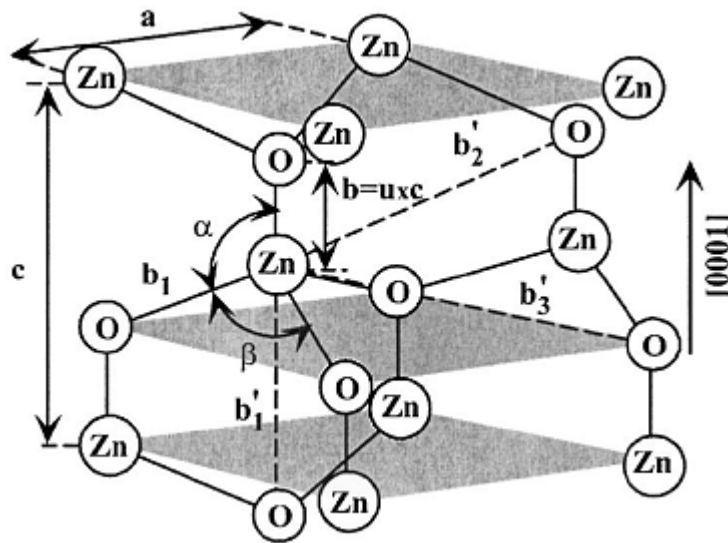
Fig. 1-1 Schematic representation of a wurtzitic ZnO structure

1.2 Introduction of the Thin Film Technology

In order to obtain good quality of ZnO thin film, Molecular beam epitaxy (MBE),

metal organic chemical vapor deposition (MOCVD)[6, 10] and pulsed laser deposition

(PLD)[11, 12] have been widely employed to grow ZnO epitaxial thin films with high

structural quality.　Recently, atomic layer deposition (ALD) has attracted much

attention for its application in ZnO growth[13].

1.3 Motivation

ALD is is a self-limiting growth process with controlled surface reaction where

the growth rate is only dependent on the number of growth cycle and the lattice

parameter of materials. ALD growth process has many advantages such as accurate

thickness control, large-area deposition, high uniformity, high reproducibility, high

covering ratio, low growth temperature, and the ability of producing sharp and

tailored interfaces[14].   Therefore, ALD is particularly suitable for the fabrication of

high quality multi quantum well (MQW) structures.

However, it is rather strange that there are very few reports on deposition of ZnO

thin films by ALD[15-17]. In this paper, ALD method is employed to fabricate ZnO

epi-films on c-plane sapphire.

1.4 Organization of this Thesis

Besides this chapter, the thesis includes other four chapters. In chapter 2 we will

show the theoretical background of the experiment such as atomic layer deposition

(ALD), atomic force microscope (AFM), scanning electron microscopy (SEM), X-ray

diffraction (XRD), Photoluminescence (PL), transmission electron microscopy (TEM).

In the chapter 3, we display the details of experiment and the measurement apparatus.

The structural characteristics and optical emission properties of the as-grown and

thermally annealed ZnO films were thoroughly studied by both scattering and

microscopic methods, including XRD,   TEM,   AFM, SEM, PL. And the effects on

thermal annealing to the structural properties are investigated in the chapter 4.   Then

we made a conclusion in the final chapter.

References:

1.   Tsukazaki, A.; Ohtomo, A.; Onuma, T.; Ohtani, M.; Makino, T.; Sumiya, M.; Ohtani, K.; Chichibu, S. F.; Fuke, S.; Segawa, Y.; Ohno, H.; Koinuma, H.; Kawasaki, M.," Repeated temperature modulation epitaxy for p-type doping and light-emitting diode based on ZnO". *Nat Mater* 2005, *4* (1), 42-46.

2.   Lim, J. H.; Kang, C. K.; Kim, K. K.; Park, I. K.; Hwang, D. K.; Park, S. J., "UV electroluminescence emission from ZnO light-emitting diodes grown by high-temperature radiofrequency sputtering". *Adv Mater* 2006, *18* (20), 2720.

3.   Smith, A., "Pyrosol deposition of ZnO and SnO2 based thin films: the interplay between solution chemistry, growth rate and film morphology", *Thin Solid Films* 2000, *376* (1-2), 47-55.

4.   Hao, X. T.; Tan, L. W.; Ong, K. S.; Zhu, F. R., "High-performance low-temperature transparent conducting aluminum-doped ZnO thin films and applications". *J Cryst Growth* 2006, *287* (1), 44-47.

5.   Shukla, R. K.; Srivastava, A.; Srivastava, A.; Dubey, K. C., "Growth of transparent conducting nanocrystalline Al doped ZnO thin films by pulsed laser deposition". *J Cryst Growth* 2006, *294* (2), 427-431.

6.   Jo, J.; Seo, O.; Choi, H.; Lee, B., "Enhancement-mode ZnO thin-film transistor grown by metalorganic chemical vapor deposition". *Appl Phys Express* 2008, *1* (4), 041202.

7.   Tang, I. T.; Wang, Y. C.; Hwang, W. C.; Hwang, C. C.; Wu, N. C.; Houng, M. P.; Wang, Y. H., "Investigation of piezoelectric ZnO film deposited on diamond like carbon coated onto Si substrate under different sputtering conditions". *J Cryst Growth* 2003, *252* (1-3), 190-198.

8.   Tena-Zaera, R.; Katty, A.; Bastide, S.; Levy-Clement, C., " Annealing effects on the physical properties of electrodeposited ZnO/CdSe core-shell nanowire arrays". *Chem Mater* 2007, *19* (7), 1626-1632.

9.   Platzer-Bjorkman, C.; Torndahl, I.; Hultqvist, A.; Kessler, J.; Edoff, M., "Optimization of ALD-(Zn,Mg)O buffer layers and (Zn,Mg)O/Cu(In,Ga)Se-2 interfaces for thin film solar cells". *Thin Solid Films* 2007, *515* (15), 6024-6027.

10.   Zhang, B. P.; Wakatsuki, K.; Binh, N. T.; Usami, N.; Segawa, Y., "Effects of growth temperature on the characteristics of ZnO epitaxial films deposited by metalorganic chemical vapor deposition". *Thin Solid Films* 2004, *449* (1-2), 12-19.

11.   Ohkubo, I.; Matsumoto, Y.; Ohtomo, A.; Ohnishi, T.; Tsukazaki, A.; Lippmaa, M.; Koinuma, H.; Kawasaki, M., "Investigation of ZnO/sapphire interface and formation of ZnO nanocrystalline by laser MBE". *Appl Surf Sci* 2000, *159*, 514-519.

12.   Liu, W. R.; Hsieh, W. F.; Hsu, C. H.; Liang, K. S.; Chien, F. S. S., "Threading

dislocations in domain-matching epitaxial films of ZnO". *J Appl Crystallogr* 2007, *40*, 924-930.

13.   Lin, C. W.; Ke, D. J.; Chao, Y. C.; Chang, L.; Liang, M. H.; Ho, Y. T., "Atomic layer deposition of epitaxial ZnO on GaN and YSZ". *J Cryst Growth* 2007, *298*, 472-476.

14.   Puurunen, R. L., "Surface chemistry of atomic layer deposition: A case study for the trimethylaluminum/water process". *J Appl Phys* 2005, *97* (12), 121301.

15.   K. Saito, Y. Watanabe, K. Takahashi, T. Matsuzawa, B. Sang, M. Kongai, Sol. Energy Mater. Sol. Cells 49 (1977) 187

16.   J. Lim, K. Shin, H.W. Kim, C. Lee, Mater. Sci. Eng., B, Solid-State Mater. Adv. Technol. 107 (2004) 301.

17.   J. Lim, K. Shin, H.W. Kim, C. Lee, Thin Solid Films 475 (2005) 256.
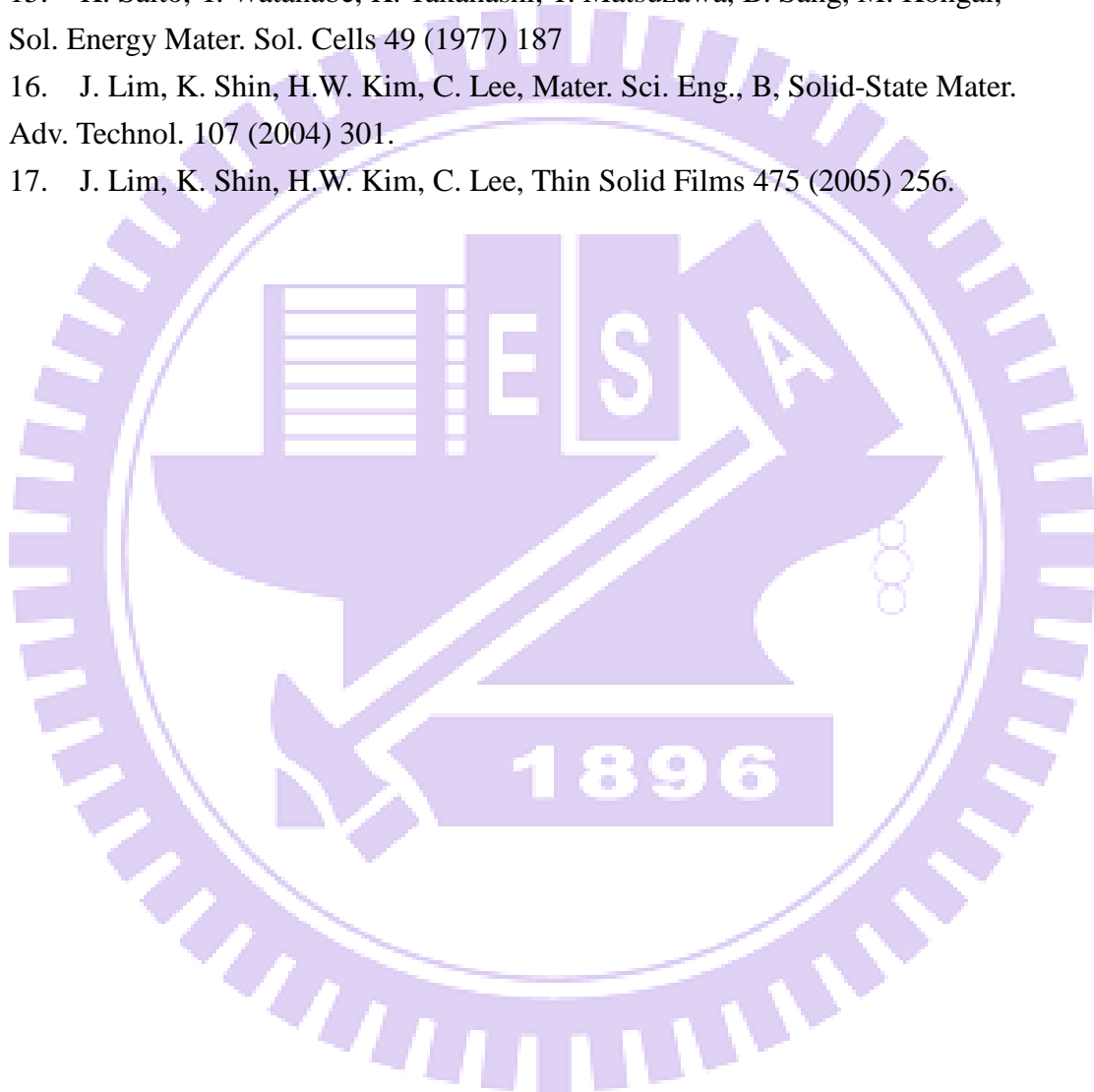
Chapter2　　Theoretical　background

2.1 Atomic Layer Deposition (ALD)[1]

Atomic Layer Deposition (ALD originally named ALE, Atomic Layer Epitaxy) was as a new deposition technique using chemical vapor deposition(CVD). It is a thin film deposition technique that is based on the sequential use of a gas phase chemical process.　Here we use Al_2O_3 as an example (Fig2-1).　First, to deposit Al layer, in step 1 and 2, Trimethyl Aluminum (TMA) reacts with the adsorbed hydroxyl groups on Si.　Until the surface is saturated with dimethyl-Aluminum complex in step 3, the extra trimethyl-Aluminum will no longer react with the hydroxyl groups. This causes the perfect uniformity of deposition Al in ALD.　Before proceeding further, the residue TMA has to be pumped out.　In step 4 and 5, H_2O reacts with the dangling methyl groups to form aluminum-oxygen (Al-O) bridges and hydroxyl surface groups.　Therefore, one cycle is finished. This cycle will be repeated over and over again to grow the desired thickness of thin film.
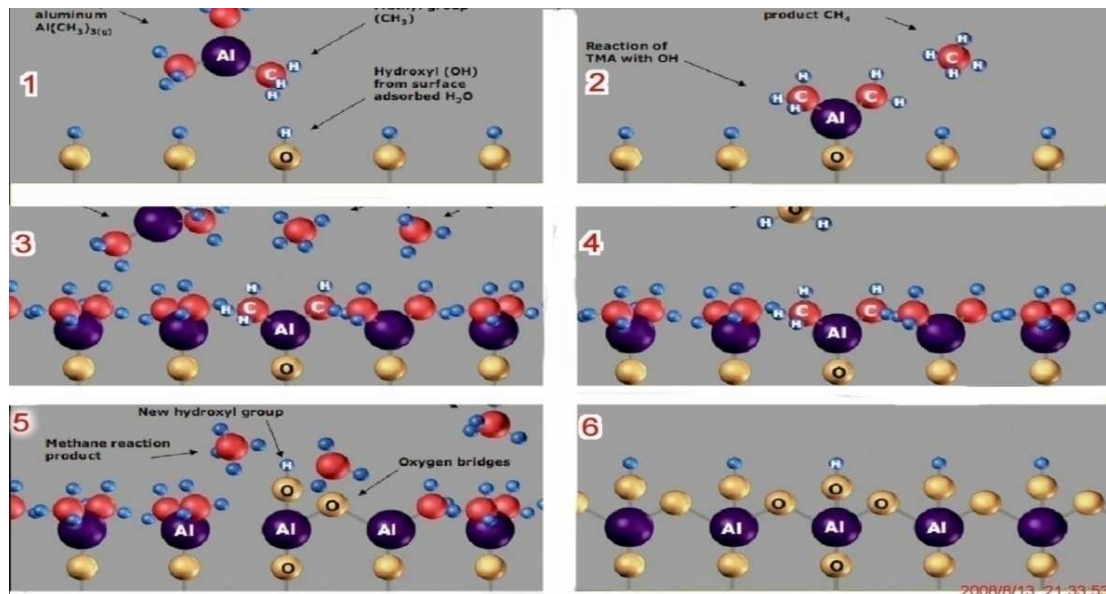
Fig. 2-1 The ALD example of the Al_2O_3 reaction. (1)(2) TMA reacts with the adsorbed hydroxyl groups; (3) Surface is saturated; (4)(5) H_2O reacts with the dangling methyl groups; and (6) One cycle finish.   [Ref. 1]

Using ALD, film thickness depends on the number of reaction cycles, which makes the thickness control accurate and simple.   This gives large area (large batch and easy scale-up) capability, excellent uniformity and reproducibility.   Also, the growth of different multilayer structures is straight forward.   These advantages make the ALD method attractive for microelectronics for manufacturing of future generation integrated circuits.   Another advantage of ALD is the wide range of film material with high density and low impurity level.   Also, lower deposition temperature can be used in order not to affect sensitive substrates such as organic substrates.

2.2 Atomic Force Microscope (AFM)[2]

The atomic force microscope (AFM) or scanning force microscope (SFM) was invented in 1986 by Binnig, Quate and Gerber. Similar to other scanning probe microscopes, the AFM raster scans a sharp probe over the surface of a sample and measures the changes in force between the probe tip and the sample. (Fig.2-2) illustrates the working concept for an atomic force microscope. A cantilever with a sharp tip is positioned above a surface. Depending on this separation distance, long range or short range forces will dominate the interaction. This force is measured by the bending of the cantilever by an optical lever technique: a laser beam is focused on the back of a cantilever and reflected into a photodetector. Small forces between the tip and sample will cause less deflection than large forces. By raster-scanning the tip across the surface and recording the change in force as a function of position, a map of surface topography and other properties can be generated.
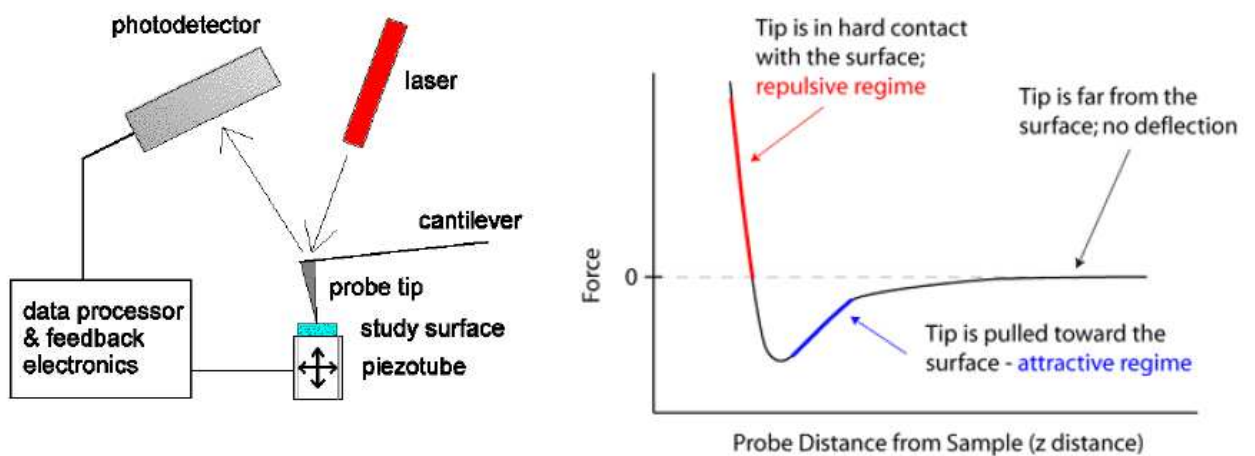
Fig. 2-2 Scheme of an atomic force microscope and the force-distance curve characteristic of the interaction between the tip and sample. [Ref. 3]

The AFM is useful for obtaining three-dimensional topographic information of insulating and conducting structures with lateral resolution down to 1.5 nm and vertical resolution down to 0.05 nm. These samples include clusters of atoms and molecules, individual macromolecules, and biologic al species (cells, DNA, proteins). Unlike the preparation of samples for STM imaging, there is minimal sample preparation involved for AFM imaging. Similar to STM operation, the AFM can operate in gas, ambient, and fluid environments and can measure physical properties including elasticity, adhesion, hardness, friction and chemical functionality.

Modes of operation for the AFM

The three general types of AFM imaging are (1) *contact mode*, (2) *tapping mode* and (3) *noncontact mode*.

1. ***Contact mode*** is the most common method of operation of the AFM and is useful for obtaining 3D topographical information on nanostructures and surfaces. As the name suggests, the tip and sample remain in close contact as the scanning proceeds. "Contact" represents the repulsive regime of the inter-molecular force curve. Most cantilevers have spring constants < 1 Nm, which is less than effective spring constant holding atoms together. One of the drawbacks of the tip remaining in contact with the sample is that large lateral forces can be exerted on the sample as the tip is dragged over the specimen. These large forces can result in deformed images and damaged samples. Small lateral forces, however, can be used to provide information on the friction (drag resistance) between the tip and sample in a mode known as *lateral force microscopy* (LFM).
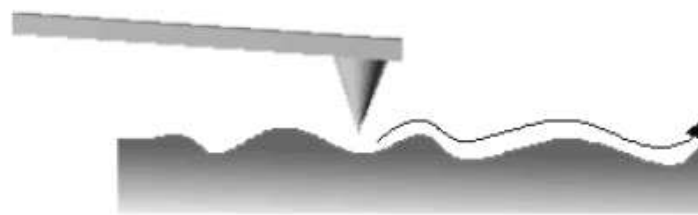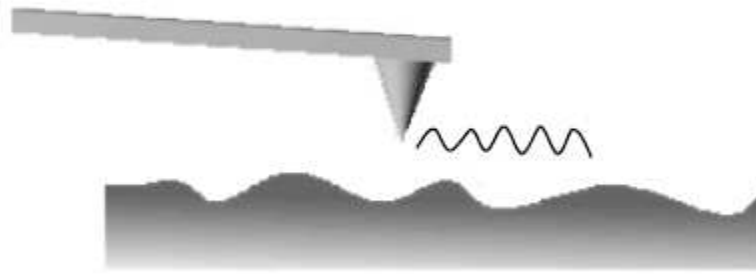

Scheme of contact mode imaging [Ref. 3]

2. ***Tapping mode*** is another mode of operation for AFM. Unlike the operation of contact mode, where the tip is in constant contact with the surface, in tapping mode the tip makes intermittent contact with the surface. As the tip is scanned over the

surface, the cantilever is driven at its resonant frequency (hundreds of kHz). Because the contact time is a small fraction of its oscillation period, the lateral forces are reduced dramatically. Tapping mode is usually preferred to image samples with structures that are weakly bound to the surface or samples that are soft (polymers, thin films).
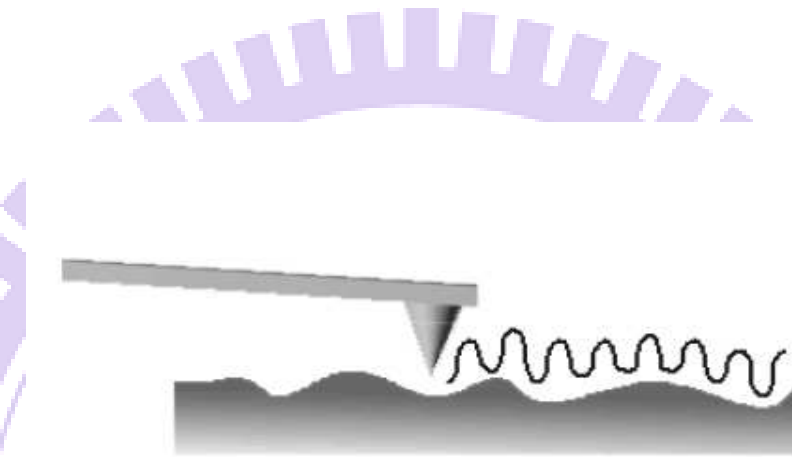
Scheme of contact mode imaging

3. *Non-contact* mode is a method where the cantilever is oscillated above the surface of the sample at distance such that it is no longer in the repulsive regime but in the attractive regime of the inter-molecular force curve. The operation of non-contact imaging is quite difficult in ambient conditions because of the existing thin layer of water on the tip and the surface. As the tip is brought close to the surface, a small capillary bridge between the tip and the sample and cause the tip to "jump-to-contact."

Scheme of non-contact mode imaging

The choice for which AFM mode to use is based on the surface characteristics of interest and on the hardness/stickiness of the sample. Contact mode is most useful for hard surfaces; a tip in contact with a surface, however, is subject to contamination from removable material on the surface. Excessive force in contact mode can also damage the surface or blunt the probe tip. Tapping mode is well-suited for imaging soft biological specimen and for samples with poor surface adhesion (DNA and carbon nanotubes). Non-contact mode is another useful mode for imaging soft surfaces.

2.3 Photoluminescence (PL)

Photoluminescence (PL) is very useful and powerful optical methods in the semiconductor industry, with its sensitive ability to find the emission mechanism and band structure of semiconductors. From photoluminescence the defect or impurity can also be found in the compound semiconductors, which affect materials quality and device performance. A given impurity produces a set of characteristic spectral

features.   The fingerprint identifies the impurity type, and often several different impurities can be seen in a single PL spectrum.   In addition, the full width of half magnitude of each PL peak is an indication of sample's quality, although such analysis has not yet become highly quantitative.[4]

Photoluminescence is the optical radiation emitted by a physical system (in excess the thermal equilibrium blackbody radiation) resulting from excitation to a nonequilibrium state by irradiation with light.   Three processes can be distinguished: (i) creation of electron-hole pairs by absorption of the excited light, (ii) radiative recombination of electron-hole pairs, and (iii) escape of the recombination radiation from the sample.   Since the excited light is absorbed in creating electron-pair pairs, the greatest excitation of the sample is near the surface; the resulting carrier distribution is both inhomogeneous and nonequilibrium.   In attempting to regain homogeneity and equilibrium, the excess carriers will diffuse away from the surface while being depleted by both radiative and nonradiative recombination processes. Most of the excitation of the crystal is thereby restricted to a region within a diffusion length (or absorption length) of the illuminated surface.   Consequently, the vast majority of photoluminescence experiments are arranged to examine the light emitted from the irradiated side of the samples.   This is often called front surface photoluminescence.

2.3.1. Fundamental Transition

Since emission requires that the system be in a nonequilibrium condition, and some means of excitation is acting on the semiconductor to produce hole-electron pairs. We consider the fundamental transitions, those occurring at or near the band edges.

1. Free excitons

A free hole and a free electron as a pair of opposite charges experience a coulomb attraction. Hence the electron can orbit about the hole as a hydrogen-like atom. If the material is sufficiently pure, the electrons and holes pair into excitons which then recombine, emitting a narrow spectral line. In a direct-gap semiconductor, where momentum is conserved in a simple radiative transition, the energy of the emitted photon is simply

$$h\upsilon = E_g - E_x$$

where E_g and E_x are the band gap and the exciton binding energy.

2. Bound excitons

Similar to the way that free carriers can be bound to (point-) defects, it is found that excitons can also be bound to defects. A free hole can combine with a neutral donor to form a positively charged excitonic ion. In this case, the electron bound to the donor still travels in a wide orbit about the donor. The associated hole which

moves in the electrostatic field of the "fixed" dipole, determined by the instantaneous position of the electron; for this reason, this complex is called a "bound exciton". An electron associated with a neutral acceptor is also a bound exciton. The binding energy of an exciton to a neutral donor (acceptor) is usually much smaller than the binding energy of an electron (hole) to the donor (acceptor).

3. Donor-Acceptor Pairs

Donors and acceptors can form pairs and act as stationary molecules imbedded in the host crystal. The coulomb interaction between a donor and an acceptor results in a lowering of their binding energies. In the donor-acceptor pair case it is convenient to consider only the separation between the donor and the acceptor level:

$$E_{pair} = E_g - (E_D - E_A) + \frac{q^2}{\varepsilon\gamma}$$

where γ is the donor-acceptor pair separation, E_D and E_A are the respective ionization energies of the donor and the acceptor as isolated impurities.

4. Deep transitions

By deep transition we shall mean either the transition of an electron from the conduction band to an acceptor state or a transition from a donor to the valence band in Fig. 2-3 Such transition emit a photon $h\upsilon = E_g - E_i$ for direct transitions and $h\upsilon = E_g - E_x - E_p$ if the transition is indirect and involves a phonon of energy E_p. Hence the deep transitions can be distinguished as (1) conduction-band-to-acceptor

transition which produces an emission peak at $h\upsilon = E_g - E_A$, and (2)

donor-to-valence-band transition which produces and emission peak at the higher
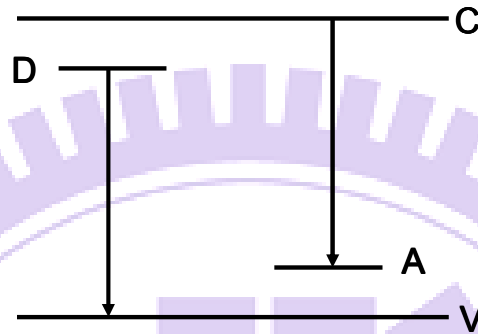
photon energy $h\upsilon = E_g - E_D$.

Fig. 2-3 Radiative transition between a band and an impurity state.

5. Transitions to deep levels

Some impurities have large ionization energies; therefore, they form deep levels

in the energy gap.   Raditive transitions between these states and the band edge emit

at $h\upsilon = E_g - E_i$. [5]

2.3.2 Influence of high excited light intensity

The photoluminescence conditions as showed before are excited by the low

excitation light intensity.   At low excitation light intensity (low density regime in

Fig.2-4) the photoluminescence optical properties are determined by single

electron-hole pairs, either in the exciton states or in the continuum.   Higher

excitation intensity (intermediate density regime in Fig.2-4) makes more excitons,

such condition would lead to the **exciton inelastic scattering processes** and form the

biexciton. The scattering processes may lead to a collision-broadening of the exciton resonances and to the appearance of new luminescence bands, to and excitation-induced increase of absorption, to bleaching or to optical amplification, i.e., to gain or negative absorption depending on the excitation conditions.   If we pump the sample even harder, we leave the intermediate and arrive at the high density regime in Fig.2-4, where the excitons lose their identity as individual quasiparticles and where a new collective phase is formed which is known as the **electron-hole plasma (EHP)**.[6]
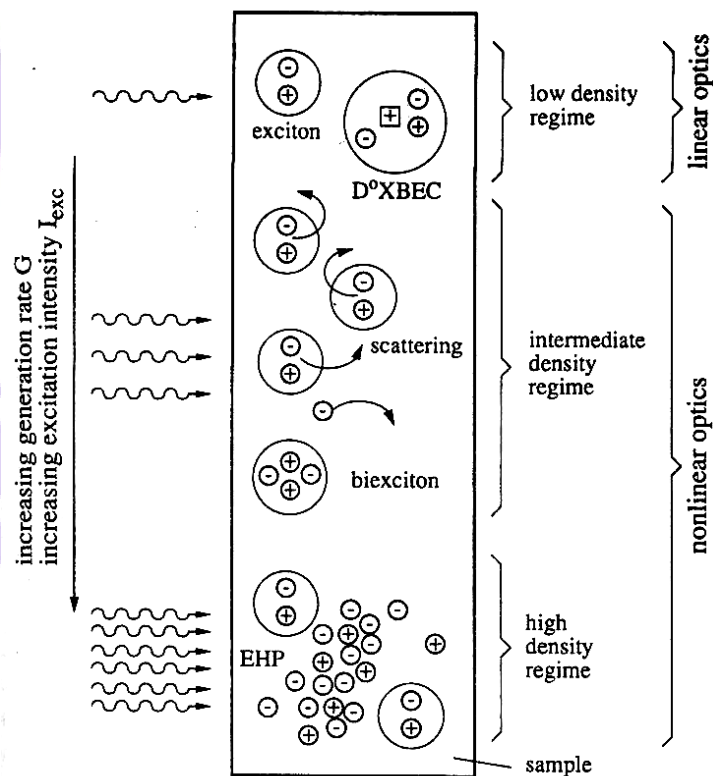

Fig. 2-4 The general scenario for many-particle effects in semiconductors [Ref. 7].

1. Scattering Processes

In the inelastic scattering processes, an exciton is scattered into a higher excited state, while another is scattered on the photon-like part of the polariton dispersion and leaves the sample with high probability as a luminescence photon, when this photon-like particle hits the surface of the sample. This process is shown schematically in Fig.2-5 and the photons emit in such a process have energies E_n given by Ref.9

$$E_n = E_{ex} - E_b^{ex}\left(1 - \frac{1}{n^2}\right) - \frac{3}{2}kT ,$$

where n=2,3,4,…, E_b^{ex} =60 meV is the binding energy of the free exciton in ZnO, and kT is the thermal energy. The resulting emission bands are usually called P-bands with an index given by n.
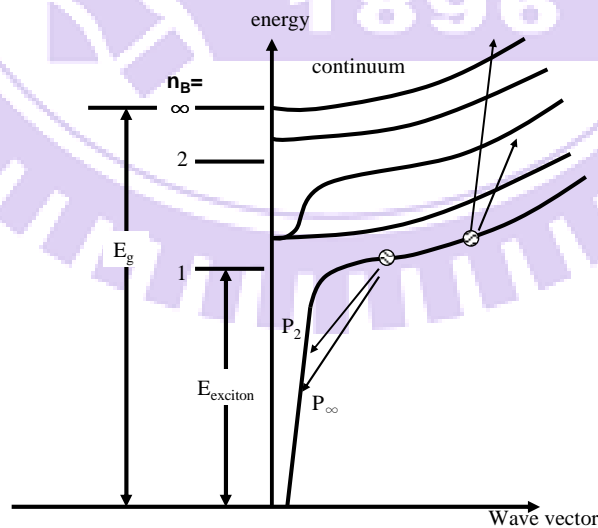

Fig. 2-5 Schematic representation of the inelastic exciton-exciton scattering processes. [Ref. 8]

2. Electron-Hole Plasma

In this high density regime, the density of electron-hole pairs n_p is at least in parts of the excited volume so high that their average distance is comparable to or smaller than their Bohr radius, i.e., we reach a "critical density" n_p^c in an EHP, given to a first approximation by

$$a_B^3 n_p^c \approx 1.$$

We can no longer say that a certain electron is bound to a certain hole; instead, we have the new collective EHP phase. The transition to an EHP is connected with very strong changes of the electronic excitations and the optical properties of semiconductors.

2.4 Scanning Electron Microscope (SEM)

The principle of the SEM, used for examining a solid specimen in the emissive mode, is closely comparable to that of a closed circuit TV system shown in Fig.2-6

In the TV camera, light from the object forms an image on a special screen, and the signal from the screen depends on the image intensity at the point being scanned. The signal is used to modulate the brightness of a cathode ray tube (CRT) display, and the original image is faithfully reproduced if Fig.2-6(a) the camera and display raster are geometrically similar and exactly in time, and Fig.2-6(b) the time for signal

collection and processing is short compared with the time for the scan move from one picture point to the next.

In the SEM the object itself is scanned with the electron beam and the electrons emitted from the surface are collected and amplified to form the video signal. The emission varies from point to point on the specimen surface and so an image is obtained. Many different specimen properties cause variations in electron emission and so, although information might be obtained about all these properties, the images need interpreting with care. The resolving power of the instrument cannot be smaller than the diameter of the electron probe scanning across the specimen surface, and a small probe is obtained by the demagnification of the image of an electron source by means of electron lenses. The lenses are probe forming rather than image forming, and the magnification of the SEM image is determined by the ratio of the sizes of raster scanned on the specimen surface and on the display screen.

For example, if the image on the CRT screen is 100mm across, magnifications of 100X and 10000X are obtained by scanning areas on the specimen surface 1mm and 10μm across, respectively. One consequence is that high magnifications are easy to obtain with the SEM, while very low magnifications are difficult. This is because large angle deflections are required which imply wide bore scan coils and other problem parts, and it is more difficult to maintain scan linearity, spot focus and

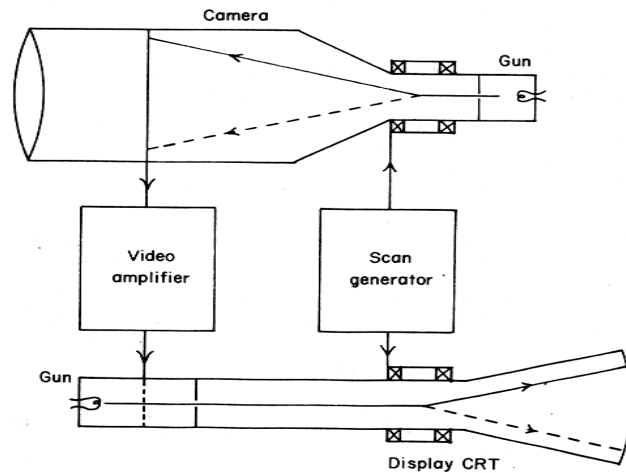efficient electron collection at the extremes of the scan.
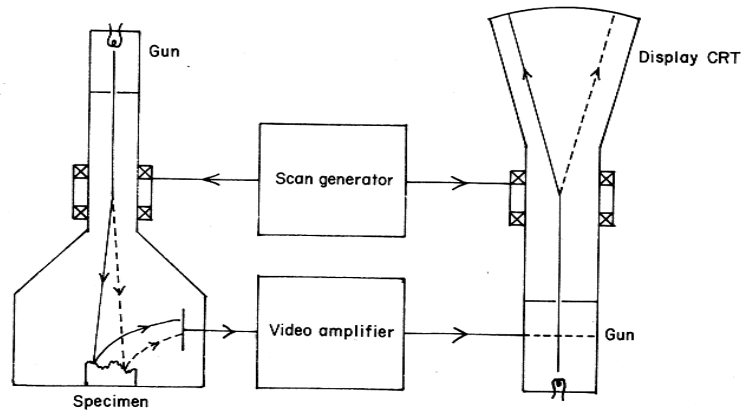

Fig. 2-6 (a) Closed circuit TV

Fig. 5.1(b). Scanning electron microscope.

Fig. 2-6 (b) Scanning electron microscope [Ref. 10].

2.5 Transmission Electron Microscope (TEM)

Transmission electron microscope (TEM) is a microscopy technique whereby a beam of electron is transmitted through an ultra thin specimen as it passes through. An image is formed from the interaction of the electrons transmitted through the specimen, the image is magnified and focused onto an image device, such as a fluorescent screen, on a layer of photographic film, or to be detected by a sensor such

as a CCD camera.

TEM are capable of imaging at significantly higher resolution than light microscopes, owing to the small de Broglie wavelength of electrons. This enables the instrument to be able to examine fine detail – even as small column of atoms, which is tens of thousand times smaller than the smallest resolvable object in a light microscope. TEM forms a major analysis method in a range of scientific fields, in both physical and biological sciences.

A modern electron microscope usually consists of an electron source and an assembly of magnetic lenses according to the scheme in Fig 2-7, where the ray path diagrams are shown in the cases when an image or a diffraction pattern (DP) are produced. The image or the DP is then displayed on a fluorescent screen or on a monitor.
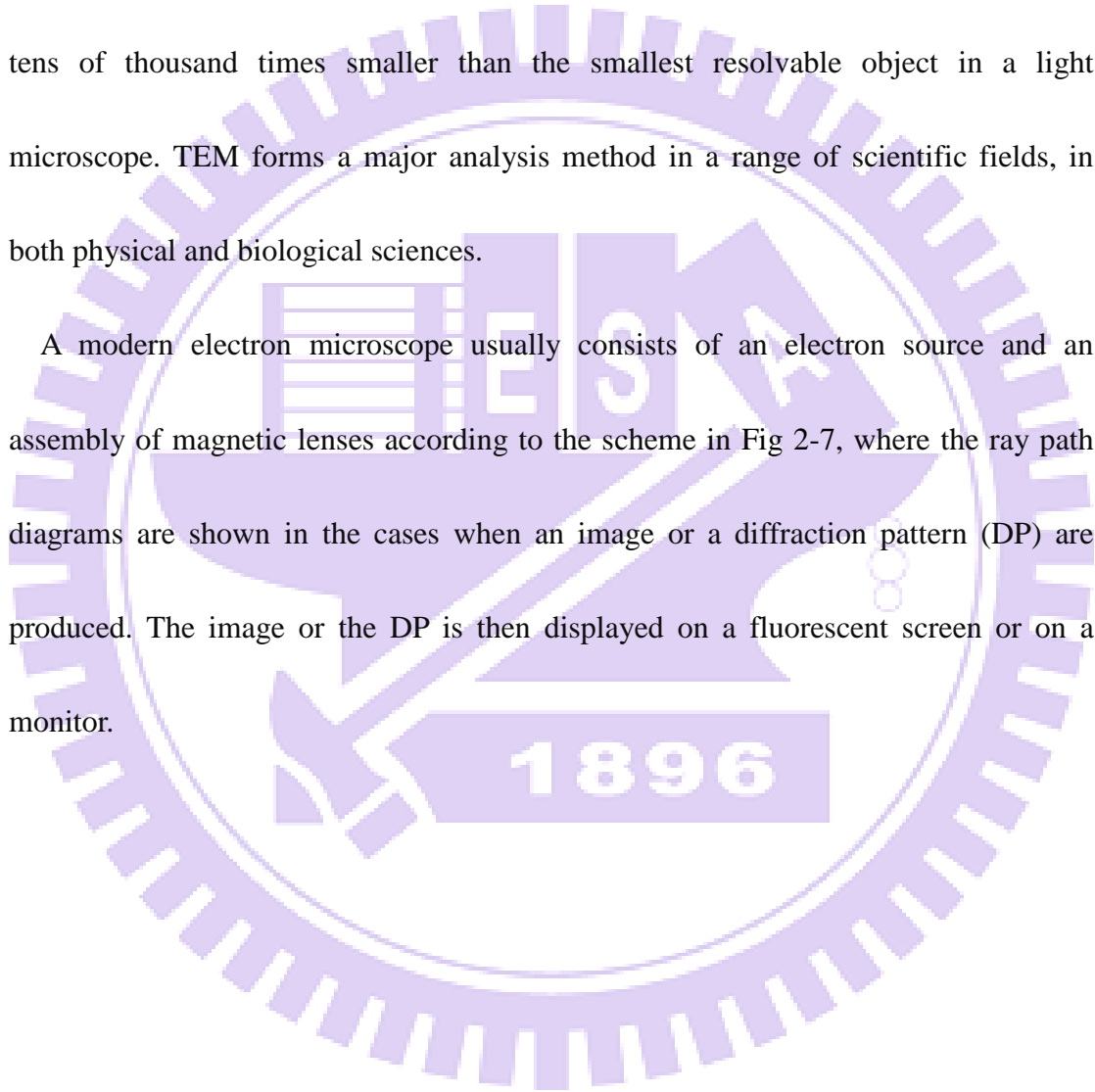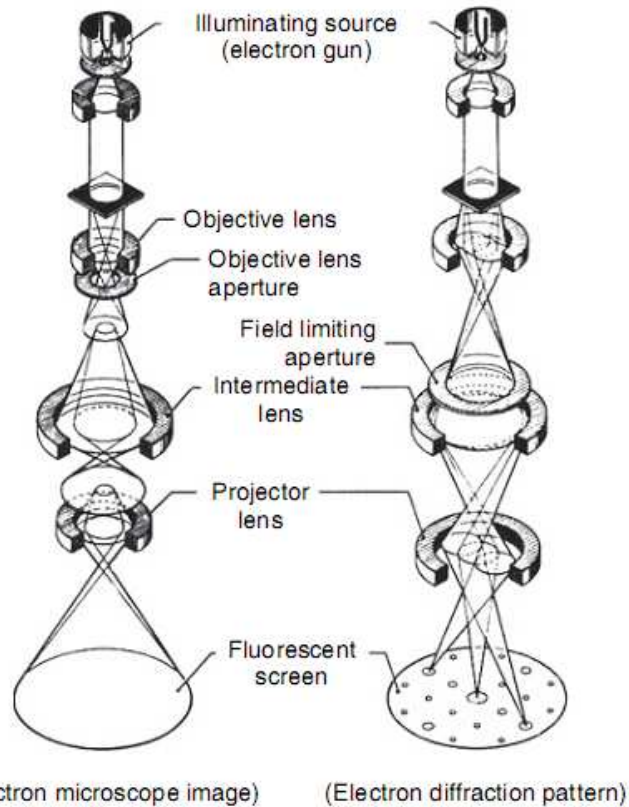
Fig. 2-7 Scheme of the lens assembly and the ray path diagram forming the image (left) or the diffraction pattern (right). [Ref. 11]

2.6 X-ray Diffraction

X-ray diffraction is a well established technique for structure determination of three-dimensional crystals. The diffracted intensity from crystal is collected by proper arrangement of diffractometer to match the Laue condition in sample reciprocal lattice. The four-circle diffractometer utilized consist of four rotatable circles, which are θ, 2θ, χ and φ circle; the 2θ circle is the detector axis controlling the magnitude of scattering vector q. The φ, χ, and θ circles control the sample orientation. When the q vector coincides with the specific reciprocal lattice vector g,

the Laue condition is satisfied. Conceptually, the φ angle is equivalent to the azimuthal angle and the χ angle is related to the polar angle of crystal.

1. Radial Scans

Radial scans collect scattered X-ray intensity while the scattering vector q is scanned along the any radial directions in reciprocal space. The most commonlyperformed radial scan is the one along sample surface normal, which is often known as the θ–2θ or ω-2θ scan as shown in Fig. 2-8. From the positions of diffraction peaks we can determine the corresponding interplanar spacing along the direction of q and the linewidth of the diffraction peak can yield the structural coherence length (grain size) and inhomogeneous strain along the same direction. Similar to the radial scans along surface-normal, radial scans along in-plane and off-normal direction for reciprocal lattice of c-oriented ZnO are shown in (a) (0002) (b) (1010) and (c) (1012) planes of Fig. 2-9, respectively. They can provide the interplanar spacing, structural coherent length along corresponding direction.
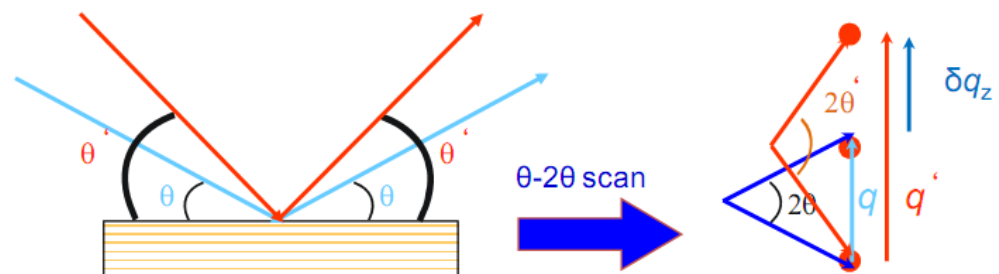

Fig. 2-8 The diagram shows the radial scan along surface normal of XRD and corresponding variation of q vector in reciprocal space.
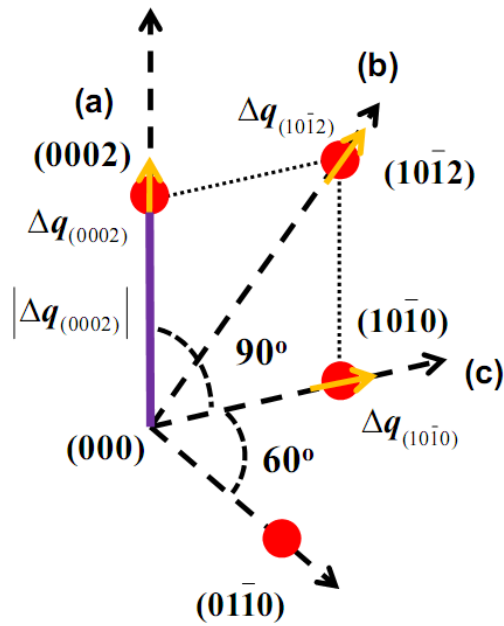
Fig. 2-9 The diagram show the reciprocal lattice for c-oriented ZnO and the radial scans along surface-normal, in-plane and off- normal direction, respectively.

2. Rocking Curve (ω-scan)

For a given incident x-ray direction and detector position, scattered x-ray collected while the crystal is rotated or called rocked through the Bragg angle θ_B. The resulting intensity vs the sample angular position θ or equivalently $\omega = \theta - \theta_B$ yields the rocking curve. The width of a rocking curve is a direct measure of the range of orientation distribution, mosaicity, present in the irradiated area of the sample because each subgrain of a typical mosaic crystal successively comes into reflecting position as the crystal is rocked, as shown in Fig. 2-10(a). Rocking curve performed at reflections along surface-normal is sensitive the tilt (polar) angle distribution of the

sample; on the other hand the rocking curved measured at surface Bragg peaks mainly reflect the twist (azimuthal) angle distribution of the sample, because the variation of scattering vector Δq is perpendicular to the radial direction of corresponding reflections, as shown in Fig. 2-10(b).
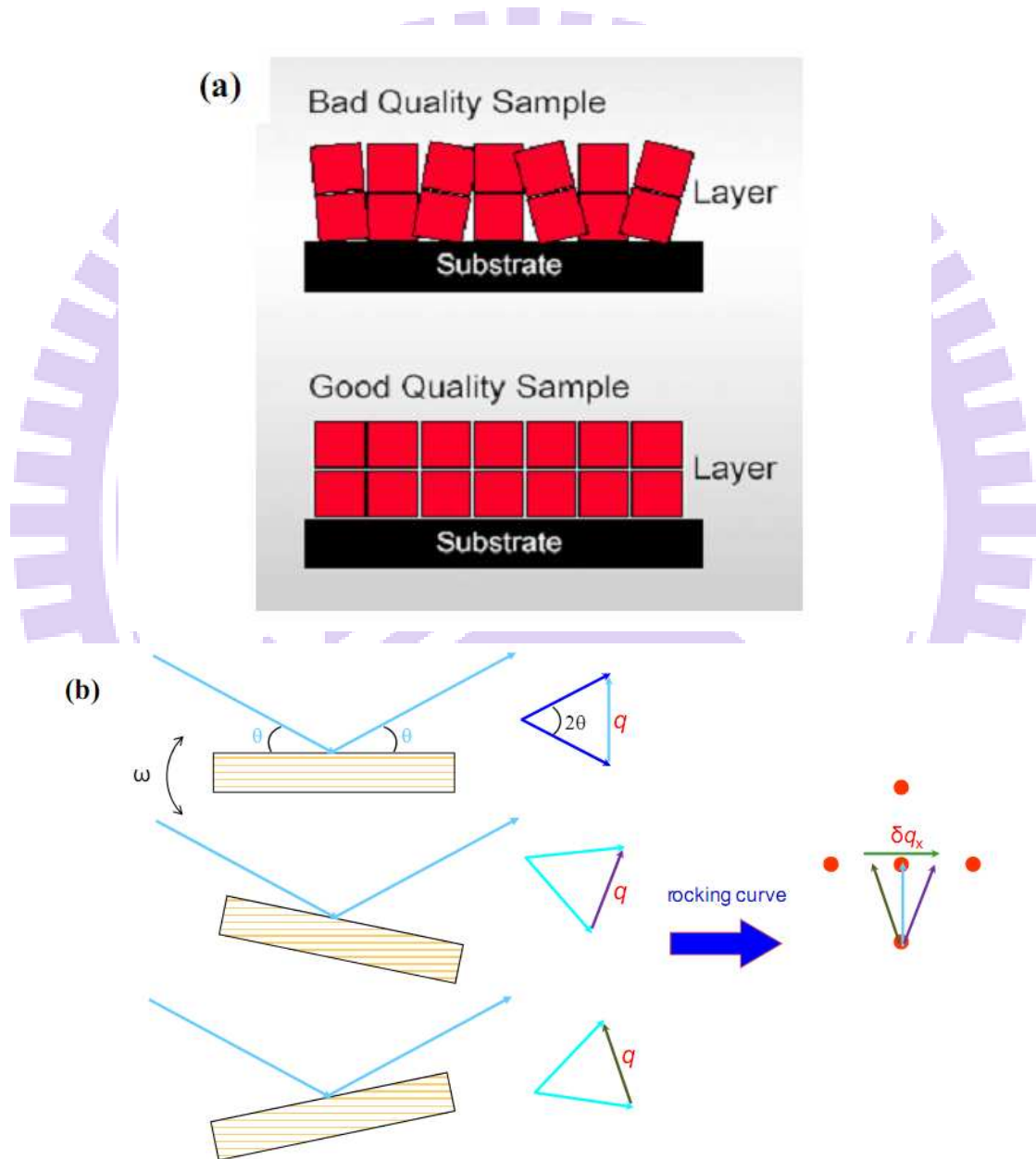

Fig. 2-10 The diagrams show the orientation distribution of subgrains of a typical mosaic crystal (a) and the rocking curve of XRD and corresponding variation of q

vector (b).

3. Azimuthal Scan

Azimuthal scan means measuring the diffraction intensity as a function of azimuthal angle φ by rotating the sample along an axis which is usually parallel to surface normal or, in some cases, to a specific crystallographic axis. Figure 2-11 illustrates schematically the reciprocal lattice of a c-oriented ZnO film. Using azimuthal scan, we can study the symmetry and crystal quality of the grown film and determine its relative orientation with substrate in epitaxy.
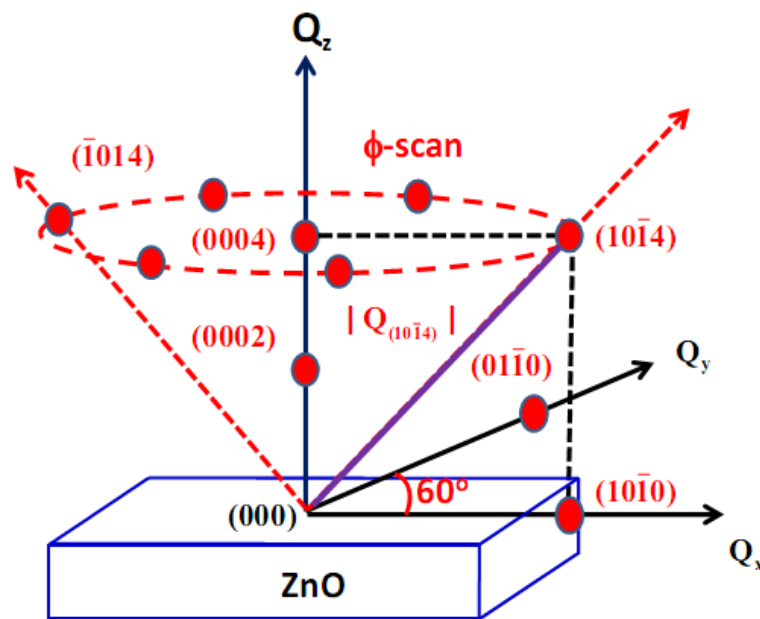

Fig. 2-11 The diagram show azimuthal scan across the off-normal ZnO(1014) peak.

References

1. http://www.cambridgenanotech.com/ald/.

2. "Scanning Probe Microscopy and Spectroscopy," R. Wiesendanger, Cambridge University Press, (1994)..

3. http://www.nanoed.org/courses

4. "Optical characterization of semiconductors: infaraed, Raman, and Pholuminescence spectroscopy" (Sidney Perlpwotz, USA,1993)p.61

5. "Optical processes in semiconductors",Jacques I. Pankove, New York, 1971, p.107

6. "Semiconductor Optics", C.F. Klingshirn, Springer, p.280

7. "Semiconductor Optics", C.F. Klingshirn, Springer, p.469

8. "Semiconductor Optics", C.F. Klingshirn, Springer, p.486

9. A.M. Morales, C.M. Lieber, *Science*, 279,208 (1998)

10. "Electron microscopy and microanalysis of crystalline materials", J.A.Belk, Applied Science Publisher,(1979)

11. "Characterization of Semiconductor Heterostructures and Nanostructures", Carlo Lamberti , Elsevier,(2008)

Chapter3　　Experimental Process Detail

3.1 Samples preparation

3.1.1 Surface treatment of the substrate

C-plane sapphire was cleaned by sequential D.I. water/acetone/D.I. water rinse

for 5min/5min/5min and then blew dry with N_2 gas.

3.1.2 The growth of ZnO thin film

The cleaned sapphire substrate was then put into the ALD reactor (SYSKEY Ltd.,

Taiwan Fig 3-1), heated to 200°C, and held at this temperature for 30 min. prior

deposition. Diethylzinc (DEZn with chemical formula of $Zn(C_2H_5)_2$) and H_2O, kept in

reservoirs at 25°C, were used as zinc and oxygen precursors, respectively.　The

growth cycle consists of precursor exposures and N_2 purge following the sequence of

$DEZn/N_2/H_2O/N_2$ with corresponding duration of 5s/15s/5s/15s.(Fig 3-2)　The

substrate temperature was maintained at 200°C under the vacuum of 1~2 torr during

the deposition.　The reaction repeated 200 times for all the studied samples.　Ideally,

two cycles of reaction yield a unit cell of ZnO along the c-axis; 200 cycles would lead

to 100 unit cells along the growth direction equivalent to a thickness of about 52 nm.
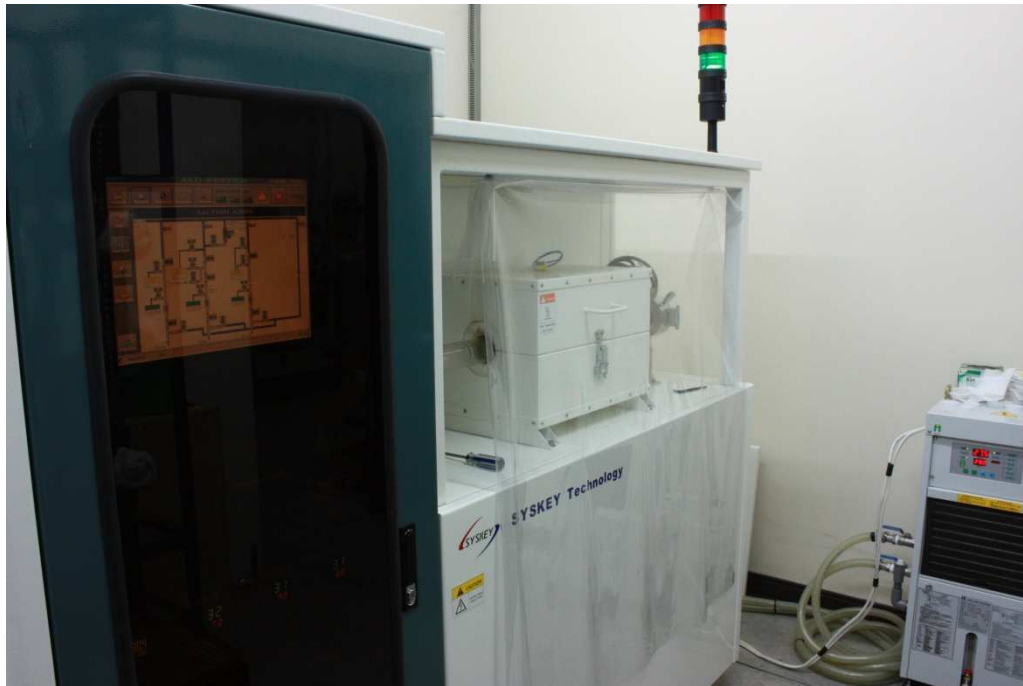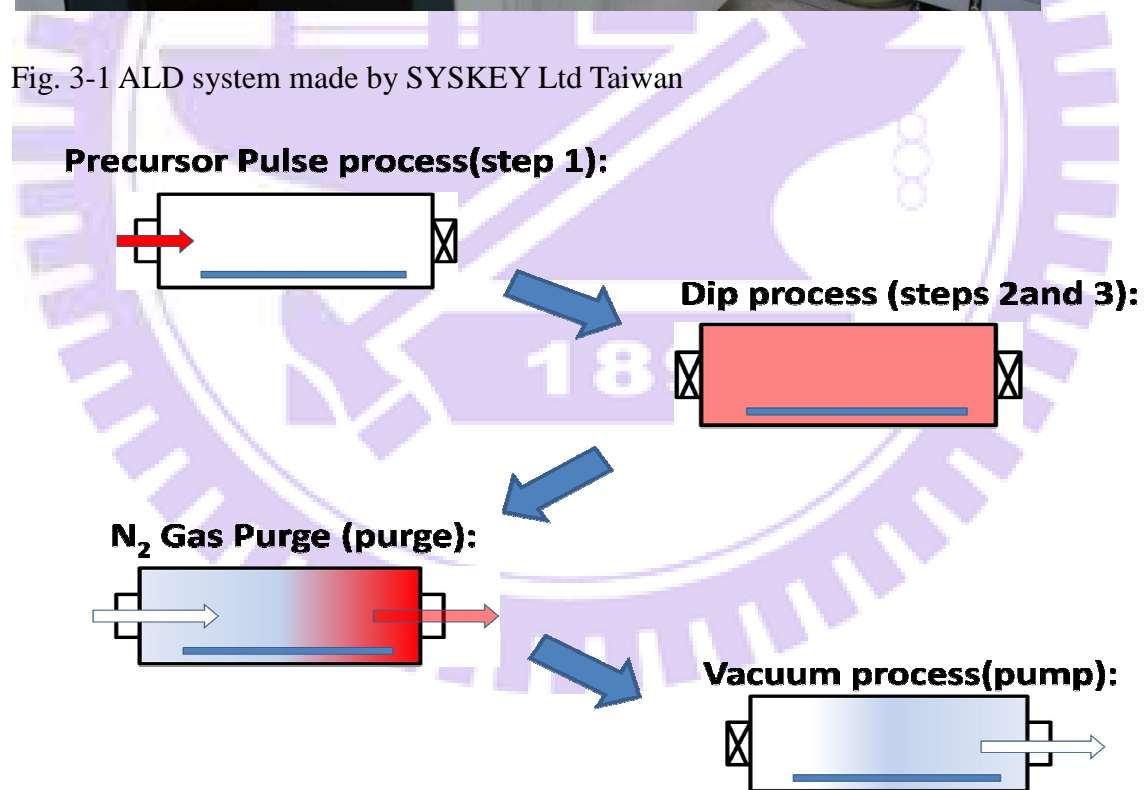

Fig. 3-1 ALD system made by SYSKEY Ltd Taiwan

Precursor Pulse process(step 1):

Dip process (steps 2and 3):

N$_2$ Gas Purge (purge):

Vacuum process(pump):

Fig. 3-2 The diagram of ALD procedure setup

3.1.3 Thermal annealing of ZnO thin film

Thermal annealing was performed at temperatures varying from 300°C, 700°C,

800°C for 1.5 hr in pure oxygen gas at 1 atm.

3.2 X-ray diffraction

The X-ray measurements were conducted using a four-circle diffractometer at beamline BL13A of National Synchrotron Radiation Research Center (NSRRC) with incident wavelength 1.02473 Å.　Two pairs of slits located between the sample and a NaI scintillation detector were employed and yielded a typical resolution of better than 5×10^{-4} nm^{-1}.

3.3 Transmission Electron Microscope system

Cross sectional TEM specimens with the thickness of about 90 ± 10 nm were prepared by focused ion beam (FIB).　TEM images were taken with a Philips TECNAI-20 field emission gun type TEM.

3.4 AFM system

Surface morphology and roughness of the ZnO layer were measured by tapping mode AFM (Veeco Dimension 5000 Scanning Probe Microscope, D5000) at National Nano Device Laboratories.

3.5 SEM system

The morphology of ZnO nanowires were observed by the Field Emission Gun Scanning Electron Microscopy (FEG-SEM)[Hitachi S-4000] at National Nano Device Laboratories. The accelerated voltage is 0.5-30kV and the magnification is 20-300k times.

3.6 Photoluminescence detection system

A UV He-Cd laser (Kimmon IK5552R-F) operating at wavelength 325nm is utilized as the pumping source for Photoluminescence (PL). Fig.3-3 shows the block diagram of PL detection system, it includes the reflective mirror, focusing and collecting lenses, and the single-grating monochromators (TRIAX 320) with a photo-multiplier tube (PMT-HVPS) which is equipped with a photon counter. The TRAIX 320 monochromator has three selectable gratings of 600, 1200 and 1800 grooves/mm. The normal applied voltage of PMT is 800 KV. We used standard fluorescent lamps to calibrate our spectral response of spectrometer and detection system. The signals of PL spectra are exposed about 0.1sec at each step of 0.1nm. The 0.1nm-resolution can be resolved with this monochromator while the entrance and exit slits are both opened about 50 m μ .

We use the HP-8453 UV-VIS spectrometer for the transmission spectra measurement. The scan range of the wavelength is from 350nm to 600nm and increment is 0.1nm. The incident light was perpendicular to the sample.
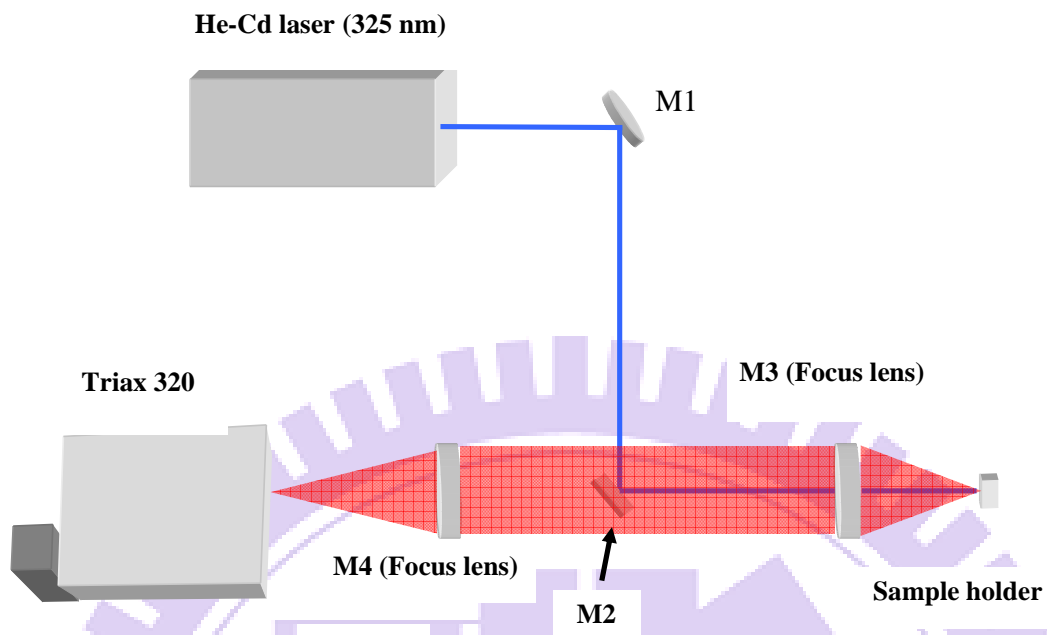
He-Cd laser (325 nm)

M1

Triax 320

M3 (Focus lens)

M4 (Focus lens)

M2

Sample holder

Fig. 3-3 PL detection system

Chapter 4 Results and discussion

4.1 Surface of the ZnO thin films

We use SEM measurement (Fig. 4-1) to observe the as-deposited ZnO thin film fabricated by ALD. It is obviously that there is thin film grown on the sapphire with sharp interface. By using the software **Image Tool** with the scale the machine given we measure the thickness of the thin film, it is about 48.295nm. The measurement data have difference with the theoretical value. (lattice constants c=5.2036 Å, (c*100)layers=52.036nm) The thickness is little less than the prediction could be attributed to the low initial growth rate. This is the results of the inhibited growth mode at the initial growth. It is mentioned in this ALD review article[1]

Through the AFM measurement (Fig. 4-2) we know the morphology of thin film is smooth. The surface root mean square (rms) roughness of the un-anneal sample is 1.6nm. It shows the ALD has the great character of high uniformity. After annealing at 800℃ the surface rms of the annealed sample become increase to about 5.7nm. The reason why the uniformity became worse is the inner reconstruction of the thin film.
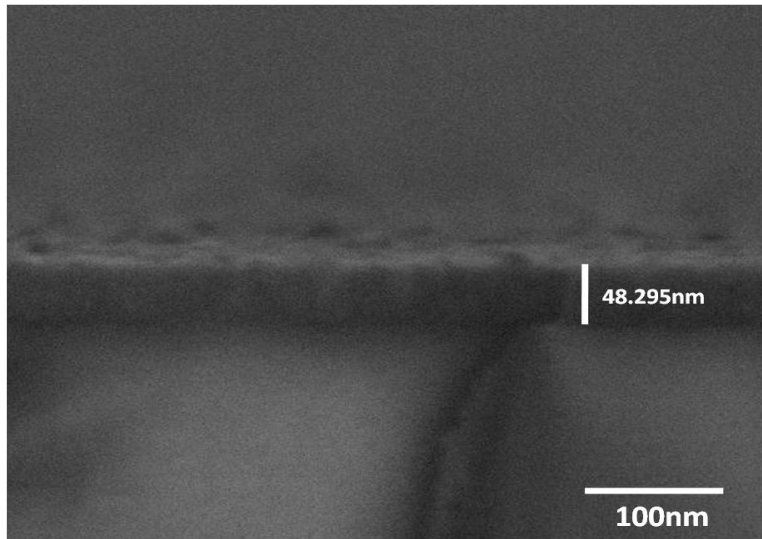
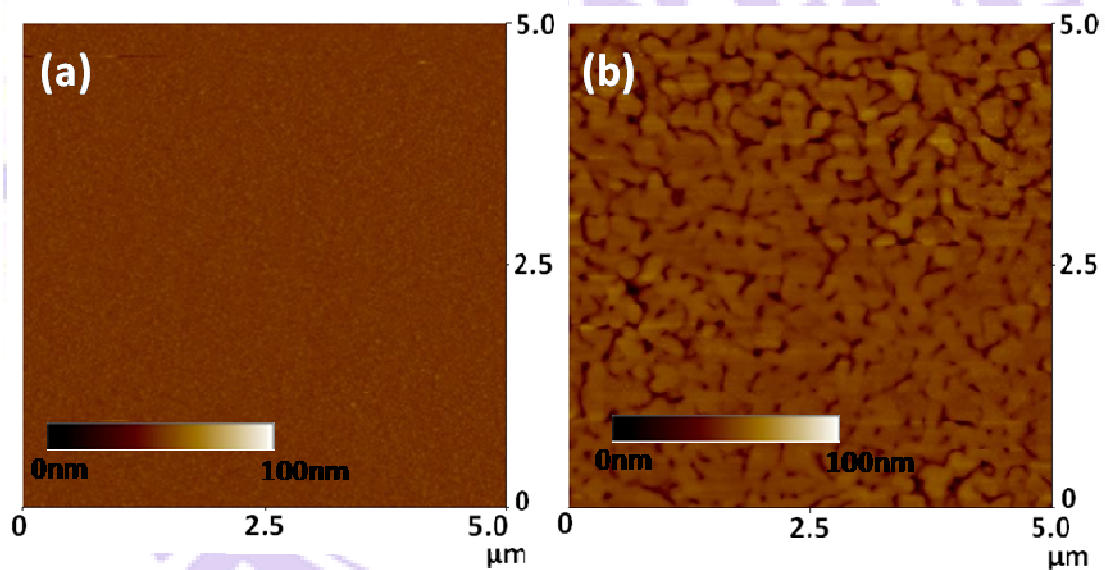Fig. 4-1 The ZnO thin film Cross-Section image of SEM

Fig. 4-2 The AFM images of the as-grwon ZnO thin film (a) before and (b) after annealing.

4.2 Results of XRD

4.2.1 θ-2θ scan

The radial scan (θ-2θ scan) along surface normal of an as-deposited ZnO layer

grown on a c-sapphire and the annealed sample at 300°C, 700°C, and 800°C is shown
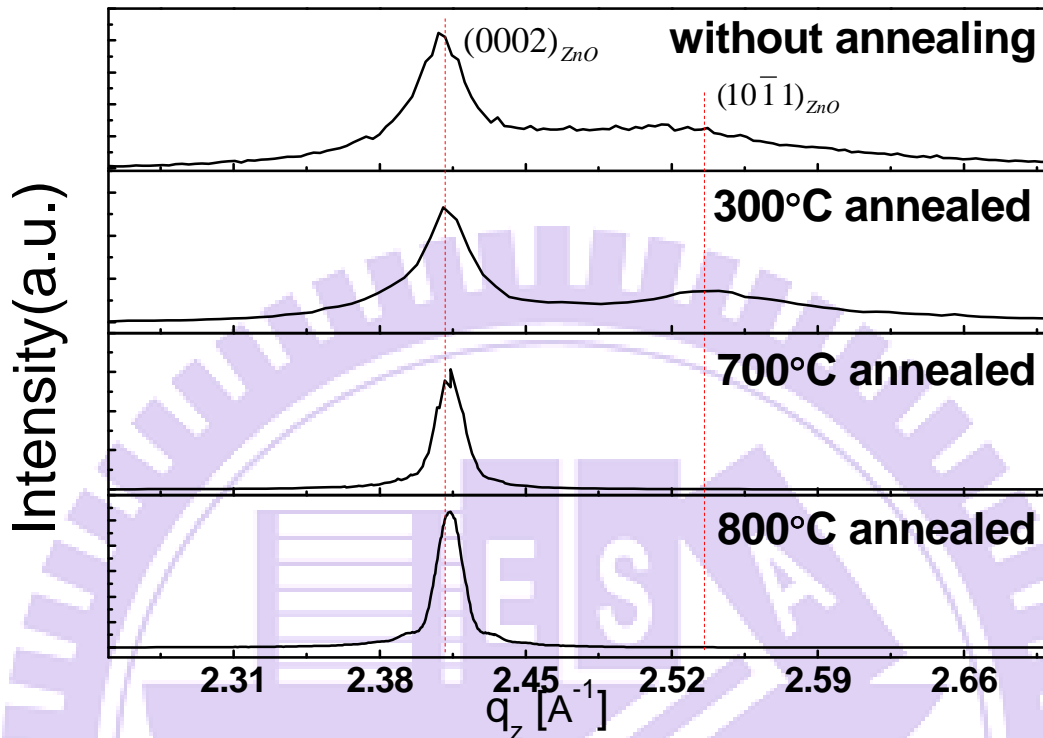
in Fig. 4-3

Fig. 4-3 The radial scan (θ-2θ scan) of the samples

The peak centered at q_z, momentum transfer along surface normal is about 2.409 Å^{-1}, and the as-deposited sample without annealing yields an interplanar spacing ~2.608 Å. This value is 0.24% larger than the d-spacing of bulk ZnO (0002) planes, d_{0002}; we thus assign this peak to ZnO (0002) reflection. At higher q_z side, a broad peak centered at ~2.53 Å^{-1} is close to $(10\bar{1}1)_{ZnO}$ reflection. Besides the reflections from sapphire substrate, no other peak generated from ZnO was observed, indicating the as-deposited ZnO layer is mainly c-plane oriented with a small fraction of $(10\bar{1}1)_{ZnO}$ -oriented domain coexisting. After thermal annealing, the $(10\bar{1}1)_{ZnO}$

reflection disappears; the peak of ZnO (0002) sharpening up and intensity enhancement of the ZnO (0002) reflection, a sign of the increase of structural coherence along the growth direction.   Moreover, the lattice parameter along c-axis systematically decreases with increasing annealing temperature as revealed by the shift of the (0002) reflection to the higher q_z value and approaches the bulk value to within 0.02% after 800°C annealing.

From the full width at half maximum (FWHM) of the ZnO (0002) reflection, the grain size is estimated by using the Scherrer's equation.   We plotted the grain size as a function of annealing temperature in Fig. 4-4.   Through the Fig. 4-4, the increasing grain size indicates the quality of ZnO film becomes better by increasing the annealing temperature from 300℃ to 800℃. The grain size of the 300℃-annealed sample did not get improvement is probably due to not high enough annealing temperature. The low annealing temperature could probably eliminate the residual hydroxyl or methyl of the ZnO film but does not have the annealing effect on ZnO film.
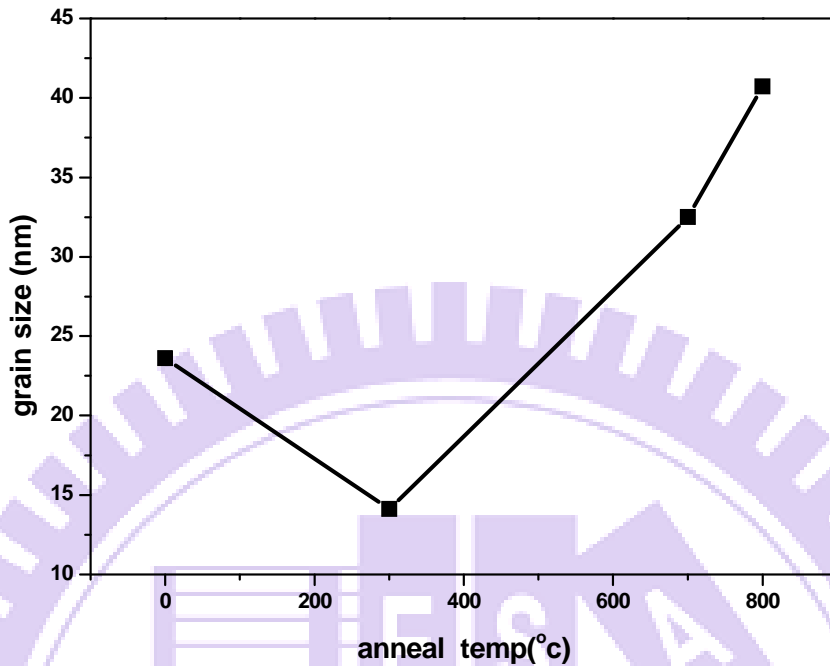
Fig. 4-4 the grain size of these samples as a function of annealing temperature.

4.2.2 The θ-scan (rocking curve)

The ZnO (0002) θ-rocking curves of the as-deposited and annealed samples are

illustrated in Fig. 4-5(a), All the curves are composed of a shape peak with typical

FWHM of less than 0.02° and a broad peak whose FWHM is two orders of magnitude

larger than the central sharp peak. The broad component is attributed to the diffuse

scattering from the structural defects, such as stacking faults and dislocations, and

misoriented grains. Such a pronounced diffuse component has hardly been observed

in ZnO epi-layers grown by PLD or MOCVD and indicates the intrinsic difference

between the structural characteristics of the ZnO layers grown by ALD and other

methods. In Fig. 4-5(b), after annealing the FWHM of the sharp component (P_S) showed mild improvement from 0.017° to 0.015°.   In contrast, the FWHM of broad component (P_B) exhibits a monotonic reduction from 2.53° for the as-deposited film to 0.91° for the 800°C annealed sample, evidencing the significant improvement of structural perfection by the thermal treatment.
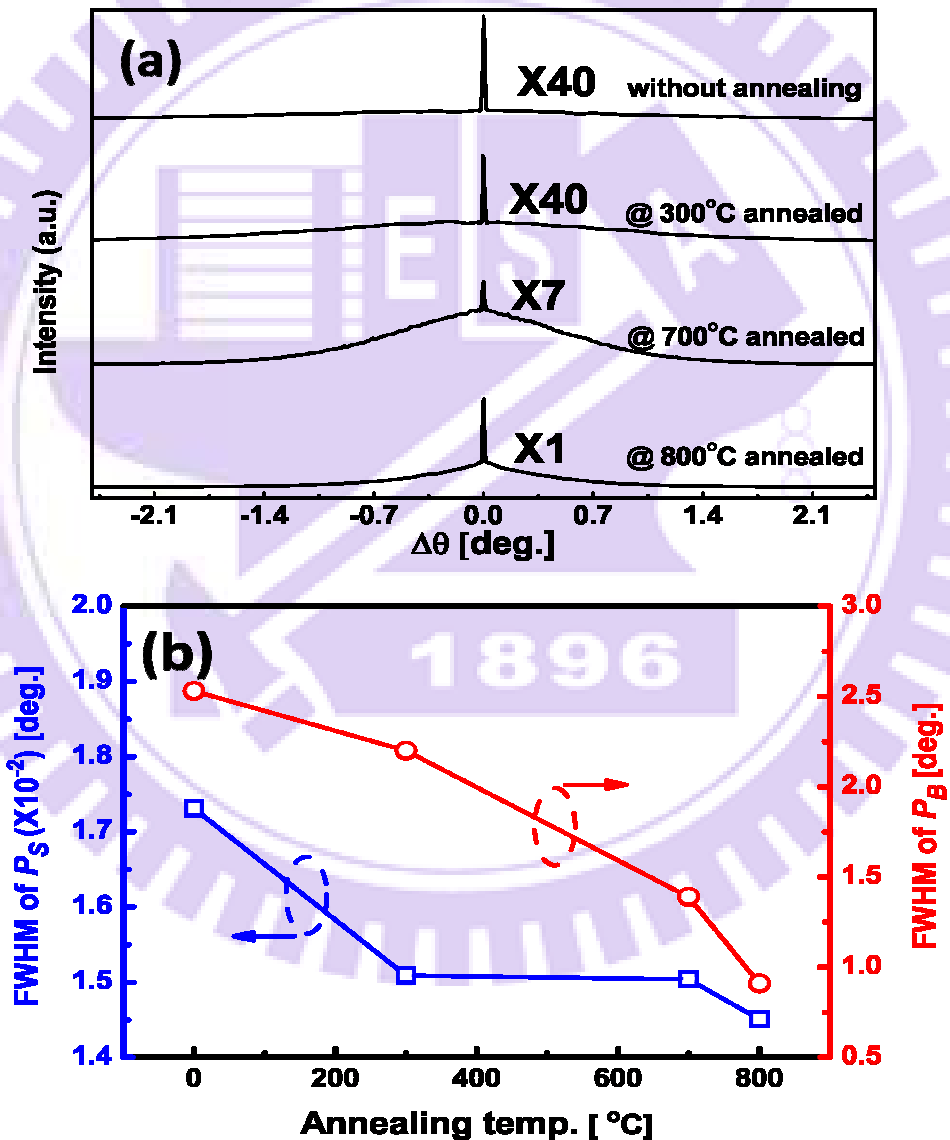

Fig. 4-5 (a) θ-rocking curves of the as-deposited and annealed samples (b) the FWHM of broad component (P_B) and sharp component (P_S)

4.2.3 The azimuthal cone scans (Φ-scans)

In order to determine the epitaxial relationship between the ZnO layers and the substrates, we performed azimuthal cone scans (Φ-scans) across the off-normal $\{10\bar{1}1\}_{ZnO}$ and $\{11\bar{2}6\}_{Al_2O_3}$ reflections, as illustrated in Fig. 4-6(a). For both as-deposited and annealed ZnO layer, the scans across the $\{10\bar{1}1\}_{ZnO}$ reflections show six-fold symmetry confirming the hexagonal symmetry. The angular positions of these peaks are offset from that of the six $\{11\bar{2}6\}_{Al_2O_3}$ reflections by 30° and presents the in-plane relationship of $\{10\bar{1}0\}_{ZnO} \parallel \{10\bar{1}0\}_{Al_2O_3}$, the "aligned orientation". It is also noticed that the FWHM of the $\{10\bar{1}1\}_{ZnO}$ peaks drastically decreases from 6.75° for the as-deposited sample to 2.48° for the sample after 800°C thermal treatment, again indicating the significant improvement in twist deformation upon annealing. Carefully examining the Φ-scan of as-deposited sample, we found another set of weak peaks with six-fold symmetry appearing at the same angular position as $\{11\bar{2}6\}_{Al_2O_3}$. This observation reveals the existence of a small fraction of c-plane ZnO has $\{10\bar{1}0\}_{ZnO} \parallel \{11\bar{2}0\}_{Al_2O_3}$ orientation, the "twisted orientation". In Fig. 4-6(b), estimated from the integrated intensity (twisted orientation: I_1, aligned orientation: I_2), the fraction of the minor twisted orientation (I_1/I_2) decreases monotonically with annealing temperature from ~4.2% in as-deposited film to ~0.03% after 800°C thermal annealing.
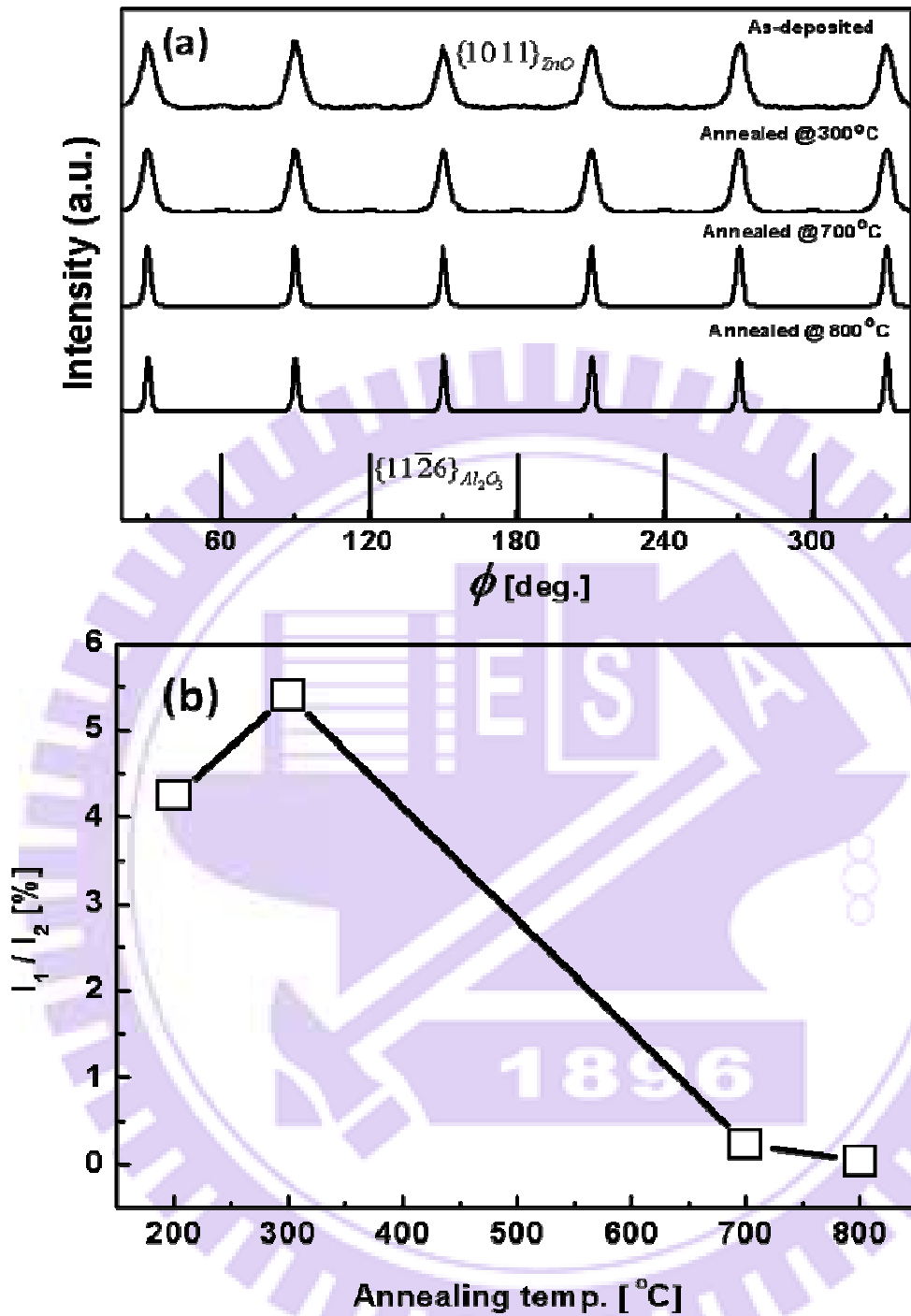
Fig. 4-6 (a) the azimuthal cone scans (Φ-scans) of samples (b) the

fraction of the minor twisted orientation (I_1/I_2)

The twisted orientation, in which the lattice of ZnO is aligned with the oxygen

sublattice in sapphire, is most commonly observed for ZnO epi-films grown on c-sapphire[2-4]. Its lattice mismatch with sapphire18.3% is smaller than the 31.8% of the aligned orientation, in which the ZnO lattice is aligned with the Al sublattice in sapphire. Intuitively, the twisted orientation is energetically favorable and indeed most of the ZnO epi-layers grown on c-plane sapphire by PLD and MOCVD, VPE have this orientation.[5-7] The aligned in-plane orientation has been reported on ZnO epi-films grown by PLD and magnetron sputtering at low deposition temperatures (T < 600°C).[8-11] The fraction of the domains with the aligned orientation increases with decreasing growth temperature and/or lower deposition rate.

The orientation of the epi-films is a result of the competition between the interfacial bonding, elastic energy and surface energy. In view of the energetics of interfacial bonding, the much larger bond energy of Al-O (511 kJ/mol) bond than the Zn-O bond (271 kJ/mol) favors the O-Al=O-Zn configuration, i.e., bonding of the O in ZnO with the Al in sapphire substrate, and leads to the alignment of Zn terminated ZnO lattice with Al sublattice. But from the aspect of smaller lattice mismatch and higher thermodynamic stability of O-terminated ZnO surface[12], the configuration with twisted orientation is preferred. I. Ohkubo *et al*. attributed the prevalence of the aligned orientation at low temperatures to Al termination of sapphire surface and the dominance of local interface energy when the growth process in kinetics limited[2, 4].

According to this argument, the low operation temperature of ALD favors the formation of observed aligned orientation but the interfacial bonding mechanism should be different because of the alternative formation of Zn and O atomic layers during two separate half reactions.

The topmost surface of a sapphire wafer after wet-cleaning is terminated by hydroxyl groups and due to its high stability it is a known difficulty of creating an OH free sapphire surface not mentioned by the mild heating pretreatment adopted in our process[13]. According to the ALD growth sequence, the zinc precursor DEZn with the chemical structure of CH_3-CH_2-Zn-CH_2-CH_3 is first supplied onto the substrate surface. One ethyl of the DEZn reacts with the hydroxyl at the sapphire surface and make the zinc atom bonded with the oxygen of the -Al=O-H to form the –Al=O-Zn-CH_2–CH_3 at the substrate surface. Volatile organic by-product Ethane is pumped away and the residual functional group ethyl prevents the continuous growth of deposited material due to the self limiting effect. Subsequently introduced H_2O reacted with ethyl group and form -Zn=O-H terminated surface[6]. After this point, the rest of the film growth can be considered as homoepitaxy. The initial bonding of DEZn to the Al atom in sapphire, –Al=O-Zn-CH_2–CH_3, anchors the orientation of the ZnO layer, which follows the orientation of the Al sublattice in sapphire and yields the observed aligned orientation $\{10\bar{1}0\}_{ZnO} \parallel \{10\bar{1}0\}_{Al_2O_3}$.

4.3 Results of TEM

It is well known that structural properties yielded by x-ray scattering are an ensemble average over the macroscopic illuminated volume, typical of mm^3. On the contrary, microscopy probes microscopic features over a much more localized region. As a complementary, we also performed TEM measurements on the ZnO epi-layers. Illustrated in Fig. 4-7(a) is a cross sectional TEM image along the $[11\overline{2}0]_{Al2O3}$ zone axis, in which ZnO grains with planes of 5.2 Å interplanar spacing parallel to the interface can be well resolved. The selected area electron diffraction (SAED) pattern (Fig. 4-7(b)) confirmed the $(0001) < 1\overline{1}00 >_{ZnO} || (0001) < 1\overline{1}00 >_{Al2O3}$ orientation in agreement with XRD observation. However, numerous defects of various kinds distribute throughout the grown film. Figure 4-7(c) is the image of 800°C annealed sample taken under the same pole; the local enlargement of the area near the ZnO/Al$_2$O$_3$ interface is shown in the inset. Drastic structural improvement was observed. Unlike the case of ZnO epi-layers grown by PLD[14] and p-MBE[7] where edge-type threading dislocations are the dominant structural defects in the film bulk, the contrast lines in the basal (0001) plane with lateral extension of the order of 10 nm (some of them are marked by arrows) are the majority of defects found in ALD grown ZnO epi-films.
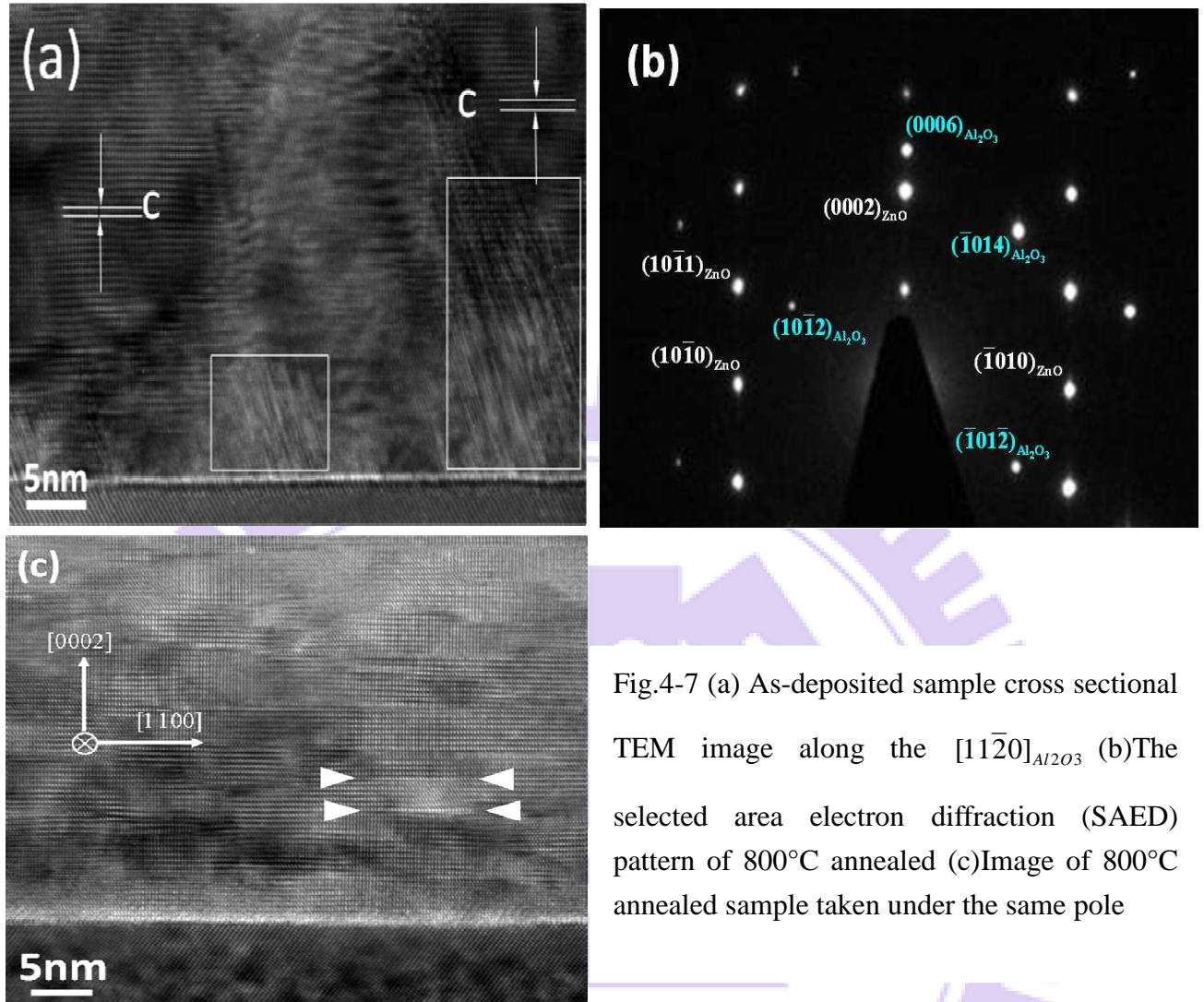
Fig.4-7 (a) As-deposited sample cross sectional TEM image along the $[11\bar{2}0]_{Al2O3}$ (b)The selected area electron diffraction (SAED) pattern of 800°C annealed (c)Image of 800°C annealed sample taken under the same pole

To characterize the nature of the lateral lines, we performed diffraction contrast analysis on the images of the 800°C annealed sample. The bright field images of the same region taken along $[11\bar{2}0]$ pole and with diffraction vector $\boldsymbol{g}$ set to (0002) $(10\bar{1}1)$, and $(10\bar{1}0)$ are shown in Figs. 4-8(a), (b) and (c), respectively. Depending on the type of error in stacking sequence or equivalently the displacement vector $\boldsymbol{R}$, which defines the relative displacement between the unfaulted lattices above and below the fault, the basal plane stacking faults in wurtzite crystal structure are

generally divided into three types: two intrinsic ones named I_1 and I_2 and an extrinsic

one named E. The displacement vectors associated with the I_1, I_2 and E type of basal

plane stacking faults are $\frac{1}{6}\langle 2\bar{2}03 \rangle$, $\frac{1}{3}\langle 1\bar{1}00 \rangle$, and $\frac{1}{2}\langle 0001 \rangle$, respectively.[15-17]

According to the extinction rules for stacking faults in TEM image, a stacking fault

will be out of contrast if the dot product of its displacement vector $\boldsymbol{R}$ with the

diffraction vector $\boldsymbol{g}$ used for imaging equals to $2\pi n$, where n = 0, ±1, ±2, … .[16, 17]

Consequently, all three types of stacking faults are visible in image with $\boldsymbol{g} = (10\bar{1}1)$

and out of contrast as $\boldsymbol{g} = (0002)$.　In the case of $\boldsymbol{g} = (10\bar{1}0)$, only intrinsic stacking

faults of types I_1 and I_2 are in contrast. Examining the images taken under different

diffraction vectors, we found about all the lateral lines visible in Fig. 4-8 (b) with $\boldsymbol{g} =$

$(10\bar{1}1)$ become out of contrast in Fig.4-8 (a) with $\boldsymbol{g} = (0002)$, confirming that basal

plane stacking faults are indeed the major structural defects in the 800°C annealed

sample. Furthermore, the absence of obvious difference in the spatial distribution of

the lines found in images taken under $\boldsymbol{g} = (10\bar{1}1)$ and $(10\bar{1}0)$, shown respectively

in Figs. 4-8(b) and (c), reveals that the stacking faults belong to intrinsic type.

Unfortunately, we cannot further verify which type of those stacking faults, I_1 or I_2.

These lines are due to limited accessible diffraction vector under experimental

geometry.

　Unlike the ZnO epi-layers grown by PLD[14] and p-MBE[7] on c-sapphire where

edge-type threading dislocations are the dominant structural defects in the film bulk, basal plane stacking faults are the majority of structural defects found in ALD grown c-ZnO epi-films. This also explains the small line width in θ-rocking curve of ZnO (0002) reflection, which is not sensitive to the basal plane stacking faults. The diversity in characteristic structural features is related to the fundamental difference in the growth mechanism of those methods. In the case of PLD deposition, a plume of materials liberated from the target, consisting of a variety of energetic species, such as atoms, ions and small clusters of the ZnO are deposited on the surface and the growth of ZnO film on c-sapphire proceeded via island nucleation followed by lateral extension.[18] Such a growth mode results in a film of a columnar structure surrounded by grain boundaries with high density of threading dislocations[14]. In contrast, the intrinsic layer-by-layer growth nature of the ALD method unfavors the initial island nucleation and suppresses the formation of threading dislocations. Apparently, 800°C annealing results in the grain growth and stimulates the precipitation of point defects such as vacancies or interstitials and/or the dissociation of dislocations together with the slip of partial dislocations, which are known as the most likely mechanisms for the generation of basal plane stacking faults.[16]
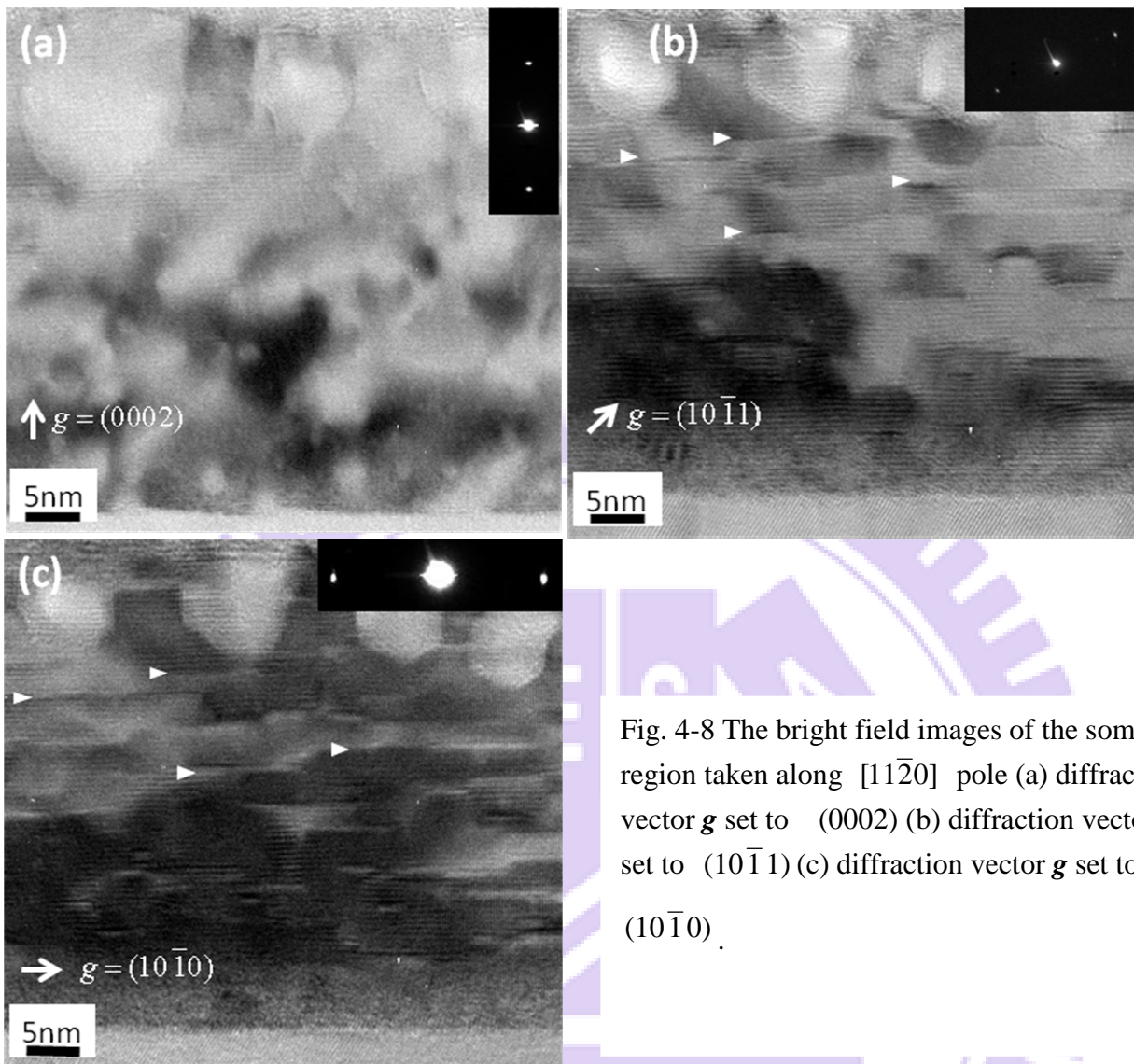
Fig. 4-8 The bright field images of the some region taken along $[11\bar{2}0]$ pole (a) diffraction vector **g** set to (0002) (b) diffraction vector **g** set to $(10\bar{1}1)$ (c) diffraction vector **g** set to $(10\bar{1}0)$.

4.4 Photoluminescence spectra

We carried out low temperature (LT) PL at 10K to characterize the optical properties of the ZnO films. The PL spectra of ZnO films are shown in Fig. 4-9. From the Fig 4-9(a) it shows the weak and broad emission peak located at the 3.22 eV with two small shoulders at the 3.316 and 3.36 eV. The Fig 4-9(b), (c) and (d) shows that after annealing the emission peak at 3.36 eV extrudes with a narrow width, this

peak is attributed to the recombination of excitons bound to neutral donor (D^0X).[20]

And the peak at about 3.31eV which is a strong emission is usually observed in many

PL spectra of ZnO material, and attributed to the recombination of the donor acceptor

pair (DAP).[21] And the followed emission peaks at about 3.25 and 3.32 eV are

attributed to the phonon replica of the DAP.   In Fig. 4-9(d), the sample annealed at

800°C reveals the D^0X emission with relative low intensity ratio comparing to the

DAP emission intensity.   In Fig 4-9(d) the peak position of the D^0X slightly shift to

high energy to 3.369 eV which could be attributed to the increasing of the free exciton

emission at 3.377 eV, and this also indicates the depressing of the oxygen vacancy.

Such phenomenon implies that the annealing temperature of 800°C could eliminate

more oxygen vacancy than 700°C annealing temperature.

From TEM and XRD measurements, it indicates that the basal plane stacking

faults are the majority of structural defects found in ALD grown c-ZnO epi-films after

annealing at 800°C, and in the Fig 4-9(d) we observed that the DAP emission is the

dominate emission.   Such observation indicates that the DAP emission comes from

the basal plane stacking fault, and is also confirmed by M. Schirra *et al*[22] which

announces that the localized acceptor states causing the 3.31 eV luminescence are

located in basal plane stacking faults and the binding energy of the 3.31 eV

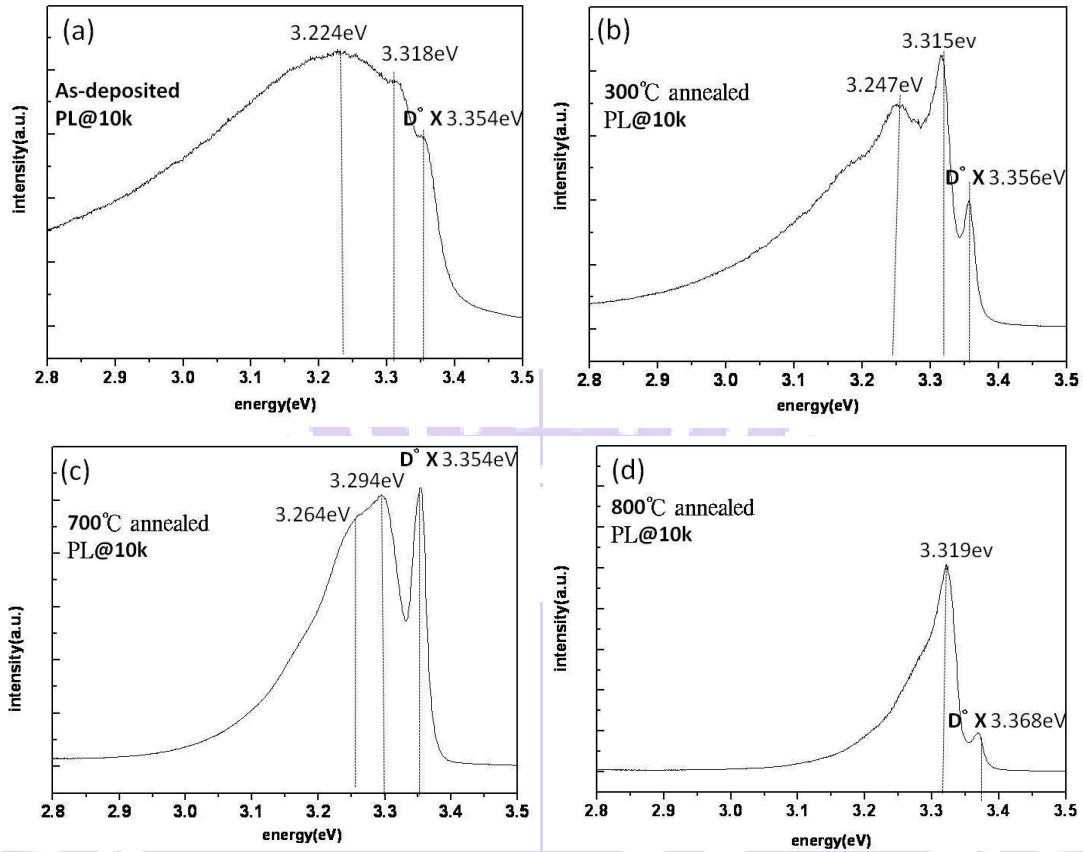luminescence was obtained to be 131meV.

Fig . 4-9 The Low temperature PL spectra at 10 k of ZnO films **(a)**the as-deposited sample **(b)** the sample annealed at 300℃ **(b)** the sample annealed at 700℃ **(b)** the sample annealed at 700℃ .

We performed the PL spectra at varied temperature from 10K to 310K in Fig. 4-10(a), and observed that the energy of the peak of 3.31 eV shifts as the temperature increasing, which was inferred that this peak consists of two emission mechanisms: DAP and free-to-bound transition (eA^0).[21] In low temperature the DAP would dominate this peak, and as the temperature raising the peak blue shifted could be attributed to the increasing of the ratio of the eA^0 emission.   Therefore we fit the binding energy (Fig. 4-10(b)) of the 3.31 eV peak at 10K PL by using the Arrhenius expression:

$$I(T) = I_0 / [1 + \alpha_1 \exp(-E_{b1}/KT) + \alpha_2 \exp(-E_{b2}/KT)].$$

The parameter of Arrhenius expression: I_0 is relative to the power of laser, α is the process rate parameter, E_{b1} is the binding energy of the eA^0, and E_{b2} is the contribution of the DAP emission.   After fitting the data the binding energy of the eA^0 is about 130.59 meV, and the E_{b2} relative to DAP is 7.592 meV.

Through the temperature dependent PL analysis, we consider that the strong emission at 3.31 eV could consists to the DAP and eA^0 emission with the binding energy of 130.59 and 7.592 meV.   The TEM images shows the mainly defect of the annealed sample is basal plane stacking, such result indicates the DAP and eA^0 emission come from these basal plane stacking fault.   Such phenomenon has also been reported by the paper M. Schirra *et al.*[22] Therefore this can explain the domination of the DAP emission at the low temperature PL in the annealed ZnO thin film deposited by ALD method.
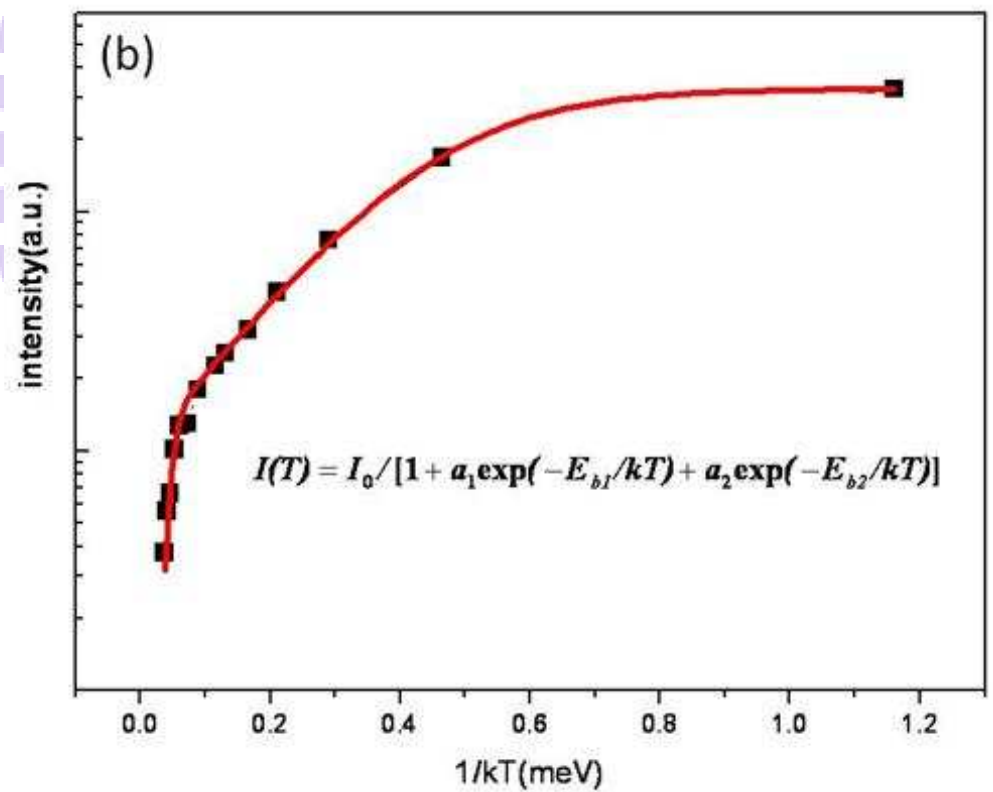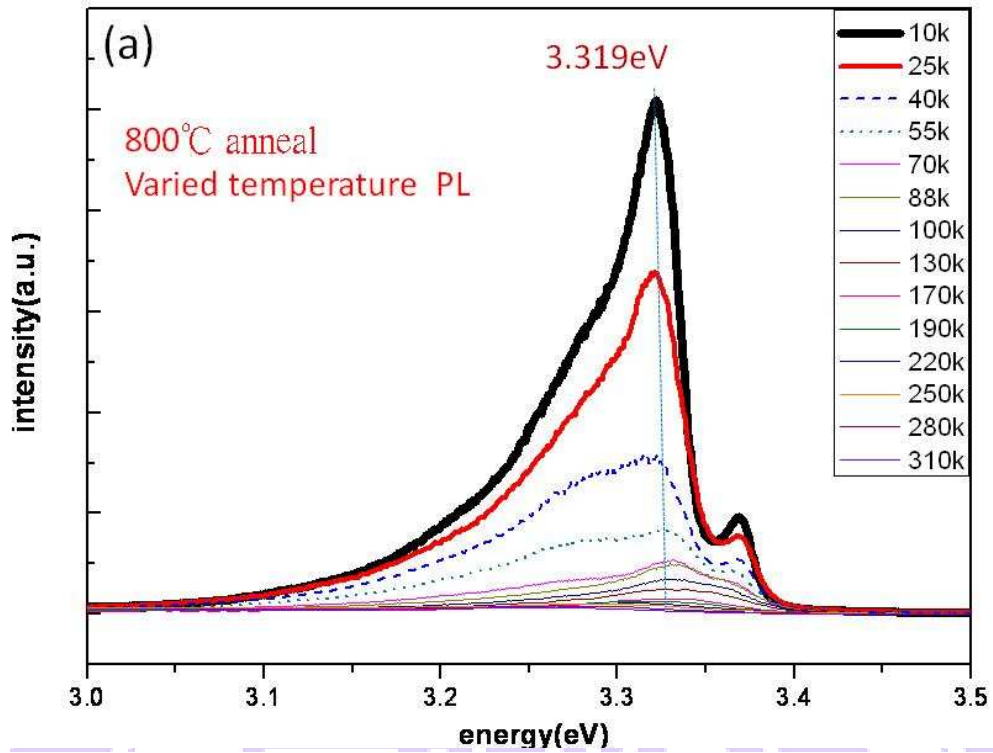
Fig. 4-10 (a) temperature dependent PL data of the sample anneal at 800℃ (b) intensity of 3.31 eV luminescence as a function of temperature

4.5 Hall measurement

Room-temperature Hall measurement was also performed to study the electrical properties of the ZnO thin films.　　We use the Van der pauw method to measure the Hall effects and use the indium (In) ball as ohm contact.　　The carrier concentration and the mobility for the as-deposited sample are 6.69×10^{19} cm^{-3} and 18.27 cm^{2}V^{-1}sec^{-1}, respectively.　　For the ZnO sample prepared by thermal annealing at 800°C, the mobility increased up to 30 cm^{2}V^{-1}sec^{-1} and the concentration down to 1.2×10^{18}cm^{-3} .　In other words, the structure of ZnO become improves and defects decrease after thermal annealing.

References:

1. Riikka L. Puurunen, "Surface chemistry of atomic layer deposition: A case study for thtrimethylaluminum/water process", JOURNAL OF APPLIED PHYSICS 97, 121301 2005

2. Koyama, T.; Chichibu, S. F., *Journal of Applied Physics* 2004, 95, (12), 7856-7861.

3. Wang, X. Q.; Iwaki, H.; Murakami, M.; Du, X. L.; Ishitani, Y.; Yoshikawa, A., *Japanese Journal of Applied Physics Part 2-Letters* 2003, 42, (2A), L99-L101.

4. Chen, Y. F.; Bagnall, D. M.; Koh, H. J.; Park, K. T.; Hiraga, K.; Zhu, Z. Q.; Yao, T., *Journal of Applied Physics* 1998, 84, (7), 3912-3918.

5. Zhang, B. P.; Wakatsuki, K.; Binh, N. T.; Usami, N.; Segawa, Y., *Thin Solid Films* 2004, 449, (1-2), 12-19.

6. Wang, X. Q.; Iwaki, H.; Murakami, M.; Du, X. L.; Ishitani, Y.; Yoshikawa, A., *Japanese Journal of Applied Physics Part 2-Letters* 2003, 42, (2A), L99-L101.

7. Chen, Y. F.; Bagnall, D. M.; Koh, H. J.; Park, K. T.; Hiraga, K.; Zhu, Z. Q.; Yao, T., *Journal of Applied Physics* 1998, 84, (7), 3912-3918.

8. Ohkubo, I.; Ohtomo, A.; Ohnishi, T.; Mastumoto, Y.; Koinuma, H.; Kawasaki, M., *Surface Science* 1999, 443, (1-2), L1043-L1048.

9. Vispute, R. D.; Talyansky, V.; Trajanovic, Z.; Choopun, S.; Downes, M.; Sharma, R. P.;

Venkatesan, T.; Woods, M. C.; Lareau, R. T.; Jones, K. A.; Iliadis, A. A., *Applied Physics Letters* 1997, 70, (20), 2735-2737.

10. Vinnichenko, M.; Shevchenko, N.; Rogozin, A.; Grotzschel, R.; Mucklich, A.; Kolitsch, A.; Moller, W., *Journal of Applied Physics* 2007, 102, (11), 113505.

11. Abouzaid, A.; Ruterana, P.; Liu, C.; Morkoc, H., *Superlattices and Microstructures* 2007, 42, (1-6), 110-115.

12. D. Kohla, M. H., and G. Heilanda, *Surface Science* 1973, 41, (2), 403-411.

13. Hass, K. C.; Schneider, W. F.; Curioni, A.; Andreoni, W., *Science* 1998, 282, (5390), 882-882.

14. Liu, W. R.; Hsieh, W. F.; Hsu, C. H.; Liang, K. S.; Chien, F. S. S., *Journal of Applied Crystallography* 2007, 40, 924-930.

15. Stampfl, C.; Van de Walle, C. G., *Physical Review B* 1998, 57, (24), R15052-R15055.

16. Gerthsen, D.; Litvinov, D.; Gruber, T.; Kirchner, C.; Waag, A., *Applied Physics Letters* 2002, 81, (21), 3972-3974.

17. Vennegues, P.; Chauveau, J. M.; Korytov, M.; Deparis, C.; Zuniga-Perez, J.; Morhain, C., *Journal of Applied Physics* 2008, 103, (8), 083525.

18. K. L.; Zhang, B. P.; Segawa, Y., *Materials Science and Engineering B-Solid State Materials for Advanced Technology* 1998, 56, (2-3), 239-245.

19. K. Thonke, T. Gruber, N. Trofilov, R. Schönfelder, A. Waag, and R.Sauer, Physica B 308–310,945 2001.

20. A. Teke, U. Ozgur, S. Dogan, X. Gu, H. Morkoc, B. Nemeth, J. Nause, and   H. O. Everitt, Phys. Rev. B 70, 195207, 2004.

21. B. P. Zhang, N. T. Binh, and Y. Segawa, Applied physics letters 83 1635 (2003)

22. M. Schirra et al.. PHYSICAL REVIEW B 77,125215 (2008)

Chapter 5   Conclusion   and   perspectives

5.1 Conclusion

ZnO epi-film fabricated by ALD has good surface uniformity. The structural characteristics of the ZnO epitaixal films on c-plane sapphire together with the influence of thermal annealing were thoroughly studied.   The d-spacing along the growth direction of the as-deposited ZnO layer is 0.24% larger than the bulk value and progressively decreases and approaches the bulk value with increasing annealing temperature. The in-plane epitaxial relationship of $\{10\bar{1}0\}_{ZnO} \parallel \{10\bar{1}0\}_{Al_2O_3}$ is confirmed from the ϕ-scan data of ZnO $\{10\bar{1}1\}$ and sapphire $\{11\bar{2}6\}$ reflections. This orientation is the same as that of ZnO grown on c-plane sapphire at low temperatures by PLD method. After annealing at high temperatures, the crystalline quality exhibits drastic improvement. TEM images reveals that intrinsic basal plane stacking faults are the dominant structural defects of the annealed ZnO thin film. In the low temperature PL at 10K of the sample annealed at 800℃ , the 3.31-eV luminescence caused by stacking faults dominating optical emission also confirmed that the stacking faults are the dominant structural defects.

5.2 Perspectives

In our research, We have successfully grown ZnO epi-film with good surface uniformity on c-sapphire substrate by using ALD. The   atomic   layer   deposition

(ALD) method brings several practical advantages such as accurate thickness-control, large area, and the ability of producing sharp and tailored interface. The growth of MgZnO ternary-alloys encounters the problem of phase separation (crystal defect). We can use ALD method to solve this problem. Because the advantages of ALD, the band gap can be tuned by just changing the thickness of layers in quasi-ternary alloy growth. In the future, if we find the great condition for growth MgO epi-film on ZnO by using ALD deposition, we can fabricate the super-lattice with artificially changeable band gap.